INFORMATION TO USERS

This manuscript has been reproduced from the microfilm master. UMI films the text directly from the original or copy submitted. Thus, some thesis and dissertation copies are in typewriter face, while others may be from any type of computer printer.

The quality of this reproduction is dependent upon the quality of the copy submitted. Broken or indistinct print, colored or poor quality illustrations and photographs, print bleedthrough, substandard margins, and improper alignment can adversely affect reproduction.

In the unlikely event that the author did not send UMI a complete manuscript and there are missing pages, these will be noted. Also, if unauthorized copyright material had to be removed, a note will indicate the deletion.

Oversize materials (e.g., maps, drawings, charts) are reproduced by sectioning the original, beginning at the upper left-hand corner and continuing from left to right in equal sections with small overlaps.

ProQuest Information and Learning
300 North Zeeb Road, Ann Arbor, MI 48106-1346 USA
800-521-0600

"SET UP OF A SHORT MAGNETIC LENS ELECTRON SPECTROMETER, AND INVESTIGATION OF Cs^{137} AND Tm^{170} DECAY."

By

Yuzuru Motoda

A THESIS

submitted in partial fulfilment of the requirement

for the degree of

MASTER OF SCIENCE

in

NUCLEAR ENGINEERING

FACULTY OF SCIENCE

UNIVERSITY OF OTTAWA

TABLE OF CONTENTS

ABSTRACT

The present work contains the discussion on the set up of a short magnetic lens electron spectrometer, and the results of an investigation of the beta decay spectra of Cs^{137} and Tm^{170}. A short magnetic lens electron spectrometer of about 21cm focal length was set up and used during the course of this investigation.

A Cs^{137} source was mainly used as a calibration source since decay spectrum is well understood. The magnetic field was varied in the range such that the electrons of 400 to 5200 gauss cm in momentum can be focussed. The spectrometer resolution of 2.16% at the K peak of Cs^{137} (624.2 KeV) and the counter resolution of 31.3% is attained. Beta decay spectra and conversion electrons of Cs^{137} and Tm^{170} were studied. Fermi-Kurie plots of Cs^{137} and Tm^{170} are presented.

CHAPTER I

INTRODUCTION

There are many ways of experimentally investigating the electrons from beta decay. These include scintillation counter method, proportional counter method, absorption method, electric and magnetic spectrometer method and so on. The magnetic spectrometer is one of the most common and useful ways of experimentally investigating beta decay. The force on the electron due to the magnetic field causes an electron to travel in an arc of a circle of radius ρ by the following relation:-

$$\frac{Bev}{c} = \frac{mv^2}{\rho} \qquad (1)$$

where, B is the strength of magnetic field in gauss, v is the velocity of an electron in cm/sec, e is the charge on electron in electrostatic unit, c is the velocity of light in cm/sec and m is the relativistic mass of electron in g. All types of magnetic spectrometers make use of this fundamental relation.

Many different types of magnetic spectrometers have been designed and developed during the past 30 years, but one can divide almost all of these into the following categories:

(1) Permanent magnet 180° deflection type,

(2) Variable field 180° deflection type,

(3) Variable field 254° deflection type,

(4) Short magnetic lens type,

(5) Double magnetic lens type,

(6) Solenoidal magnetic lens type,

(7) Magnetic lens ring focussing type.

The 180° or 254° deflection types are suitable for the experiments requiring high resolution, especially using 254° type, one can get even 0.01% resolution.

The spectrometer used in our experiment belongs to the single lens group. An air cored short magnetic lens of the type shown in Fig. 1, in a simplified form has focussing properties for a beam of electrons. The beta source is indicated by S in the Fig. 1. A magnet coil is equiped with water cooling channels and contains approximately 3600 turns of copper wire. With a given current through the coil which is controlled by the helipot setting, only electrons of a certain momentum will be focussed onto the detector C. Pulses produced in the detector, then, will be amplified by the head amplifier and be sent into single channel pulse height analyzer, where the noise pulses are discriminated and the true pulses are counted with the aid of a scaler. The chamber is kept in a good vacuum with 2 types of vacuum

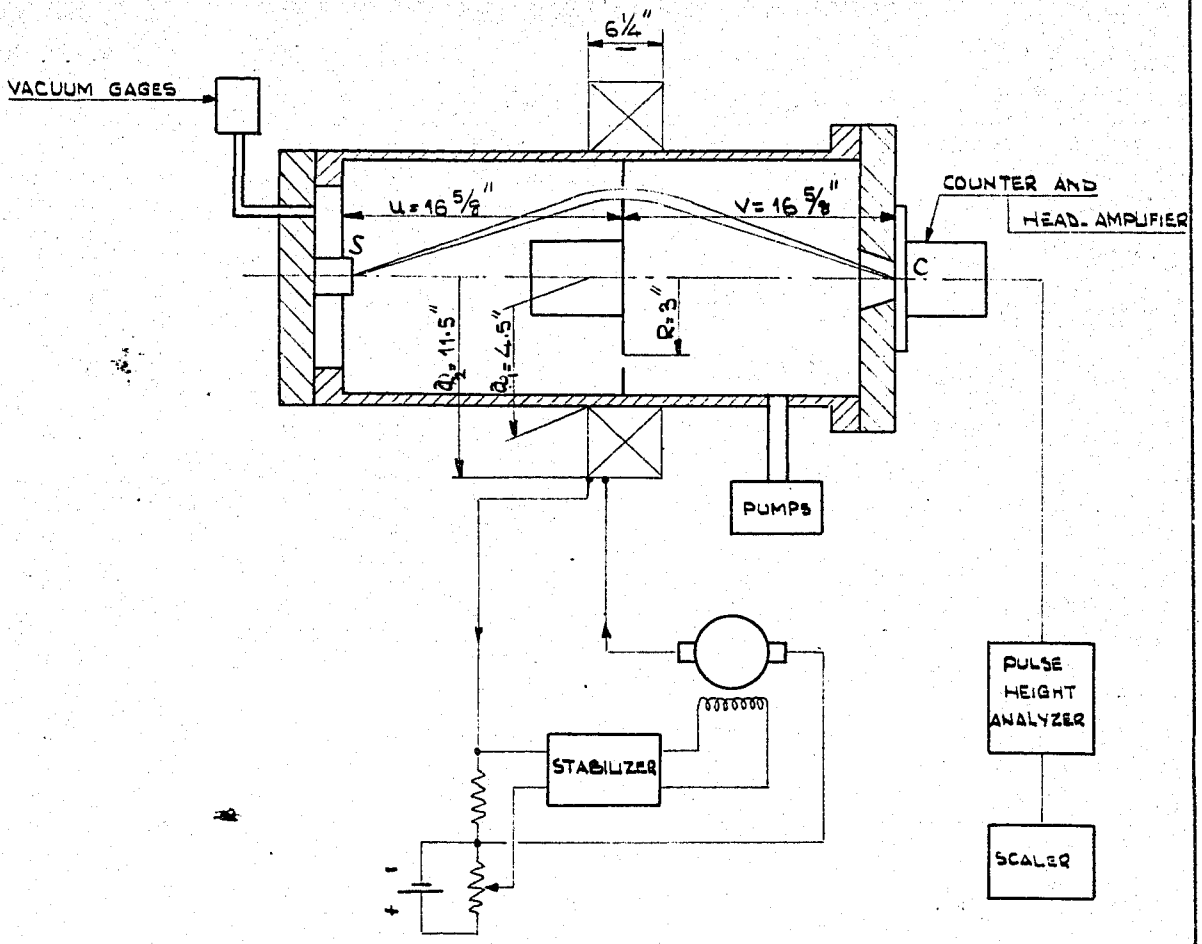

Fig. 1. Simplified diagram of short magnetic lens electron spectrometer

pumps. The vacuum gauges are attached at the source end of the chamber by which the degree of vacuum is measured. The current for the coil is obtained from a DC generator controlled by a current stabilizer.

CHAPTER II

HISTORICAL REVIEW

The field of beta ray spectroscopy rather belongs to the classical domains of nuclear physics, and an abundance of excellent reviews on beta ray spectroscopy is available. This field can be traced back to more than 40 years ago. The first 30 years of beta ray spectroscopy were consumed in establishing the general characteristics of beta ray spectra.

In 1934, Fermi provided a successful theory of the shape of beta ray spectra and the lifetime of beta ray sources. Details of these will be found in the later paragraph of the present paper.

At the end of 1930's and the beginning of the 1940's when artificially produced isotopes became available, the domain of nuclear spectroscopy grew tremendously.

In 1910 the first determinations of the energies of beta particles by their deflection in a magnetic field were carried out by von Baeyer and Hahn. But since they employed the so-called "direct deflection method", and no focussing of beta rays was used, both the transmission and the resolution were very poor.

The first magnetic focussing device is due to Danysz who in 1912 suggested the semicircular focussing

principle. Later, in 1935, the use of the "chromatic aberration" of a short magnetic electrons lens for the analysis of beta ray spectra was proposed first by Kiemperer. In 1944, Deutsch et al (1) successfully applied this type of spectrometer. Since then, together with the theory of the shape of beta ray spectra by Fermi, magnetic lens type spectrometers have been used by many people to investigate the beta ray spectra.

During the 1940's great efforts were made to improve the instruments with which the experimental data of higher qualities were obtained.

Deutsch et al (1) derived the relation

$$(n\ i/p)^2 = 6.72 \qquad (2)$$

between the number of ampere turns ni and the momentum p in gauss cm of the electrons to be focussed.

CHAPTER III

THEORETICAL PRINCIPLES

The purpose of this chapter is to present a review of the theories which have been applied to set up the spectrometer and to carry out the experiment, and that of the theories of beta decay spectra of Cs^{137} and Tm^{170}.

A. Magnet Current Stabilizer

The magnet coil must be supplied with a very steady current free from ripple in order to get the stable magnetic field. Fig. 2 shows the circuit diagram of our magnet current stabilizer which was provided for us. The amplifier circuit amplifies the difference between the voltage developed across the 0.5 Ω resistor and the voltage on the helipot. Compartment (1) in Fig. 2 converts this difference to 400 cycle AC by chopper tube, the compartment (2) amplifies this AC, and then rectifies it in a phase sensitive detector (compartment 3) to control the grids of 6AS7 tubes. Sixteen 6AS7 tubes are used in parallel to control the generator field. The whole system operates by keeping the difference between the voltage developed across the 0.5 Ω , i.e., I x 0.5 volts, and the reference voltage

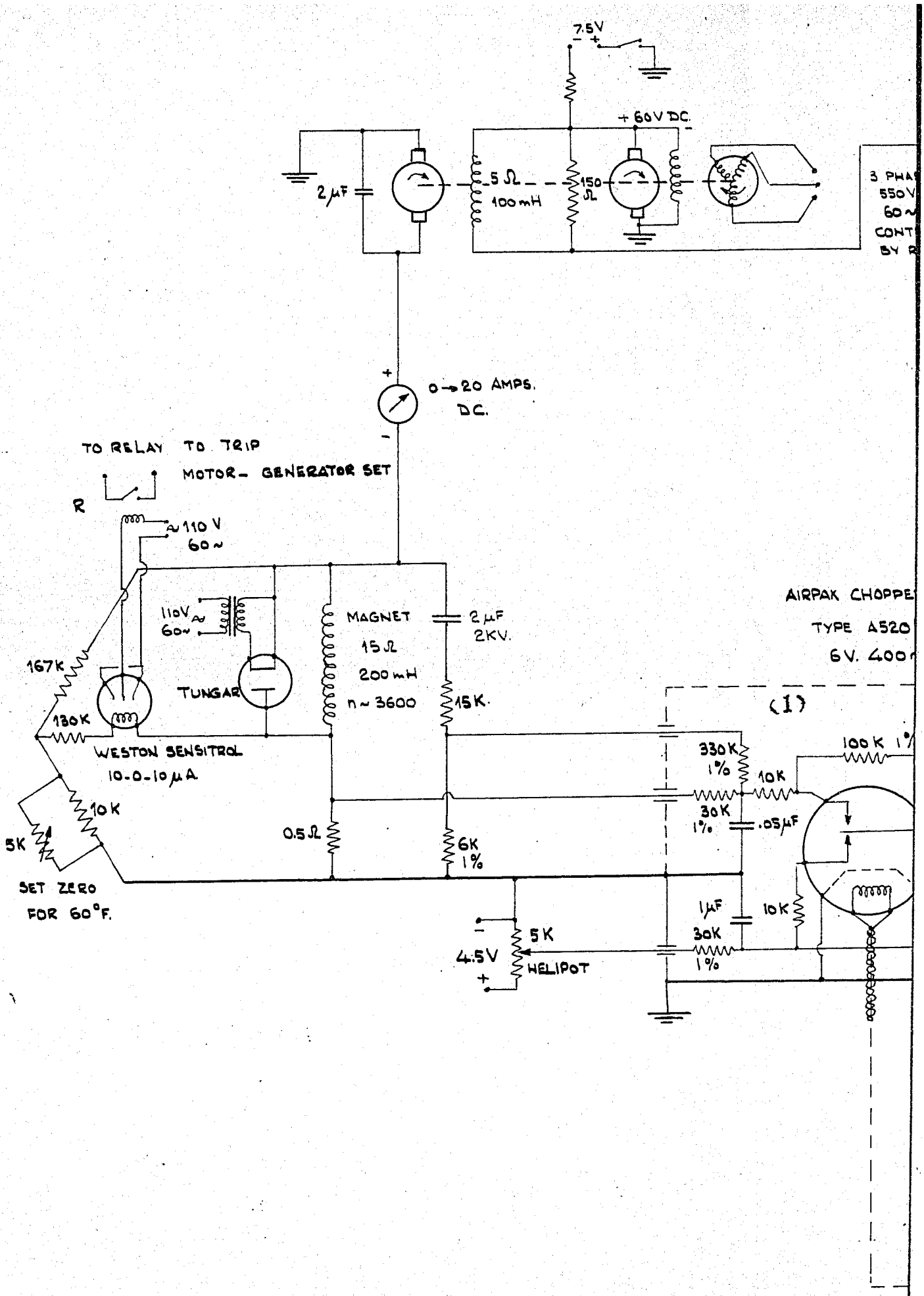
7.5V
+ 60V DC.
2 μF
5 Ω
100 mH
150 Ω
3 PHA
550V
60~
CONT
BY R
0 → 20 AMPS.
DC.
TO RELAY TO TRIP
MOTOR - GENERATOR SET
R
~110 V
60~
110V ~
60~
MAGNET
15 Ω
200 mH
n ~ 3600
2 μF
2KV.
15K.
167K
130K
TUNGAR
WESTON SENSITROL
10-0-10 μA
10K
5K
SET ZERO
FOR 60°F.
0.5 Ω
6K
1%
AIRPAK CHOPPE
TYPE A520
6V. 400
(1)
330K
1%
10K
30K
1%
.05μF
100K 1%
1μF
10K
30K
1%
5K
4.5V
HELIPOT

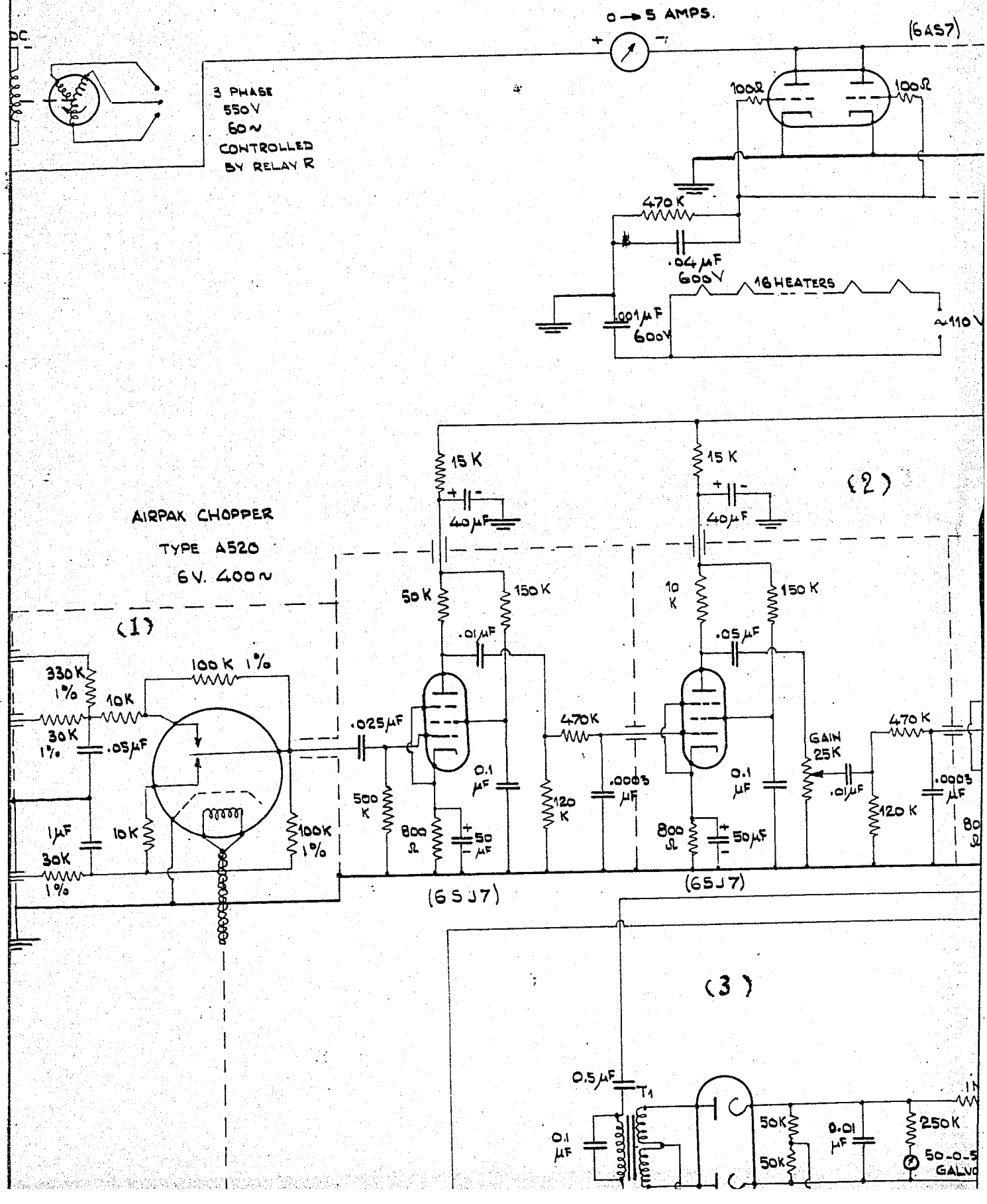
0 → 5 AMPS.
+
−
(6AS7)
DC.
3 PHASE
550V
60~
CONTROLLED
BY RELAY R
100Ω
100Ω
470K
.04μF
600V
16 HEATERS
.001μF
600V
~110V
AIRPAK CHOPPER
TYPE A520
6V. 400~
(1)
(2)
(3)
15 K
40μF
50 K
150 K
.01μF
10 K
.05μF
330K
1%
10K
30K
1%
.05μF
100K 1%
.025μF
470K
GAIN
25K
.01μF
120 K
.0003
μF
0.1
μF
500
K
800
Ω
50
μF
1μF
10K
30K
1%
100K
1%
(6SJ7)
(6SJ7)
0.5μF
T1
0.1
μF
50K
50K
0.01
μF
250K
50-0-5
GALVO

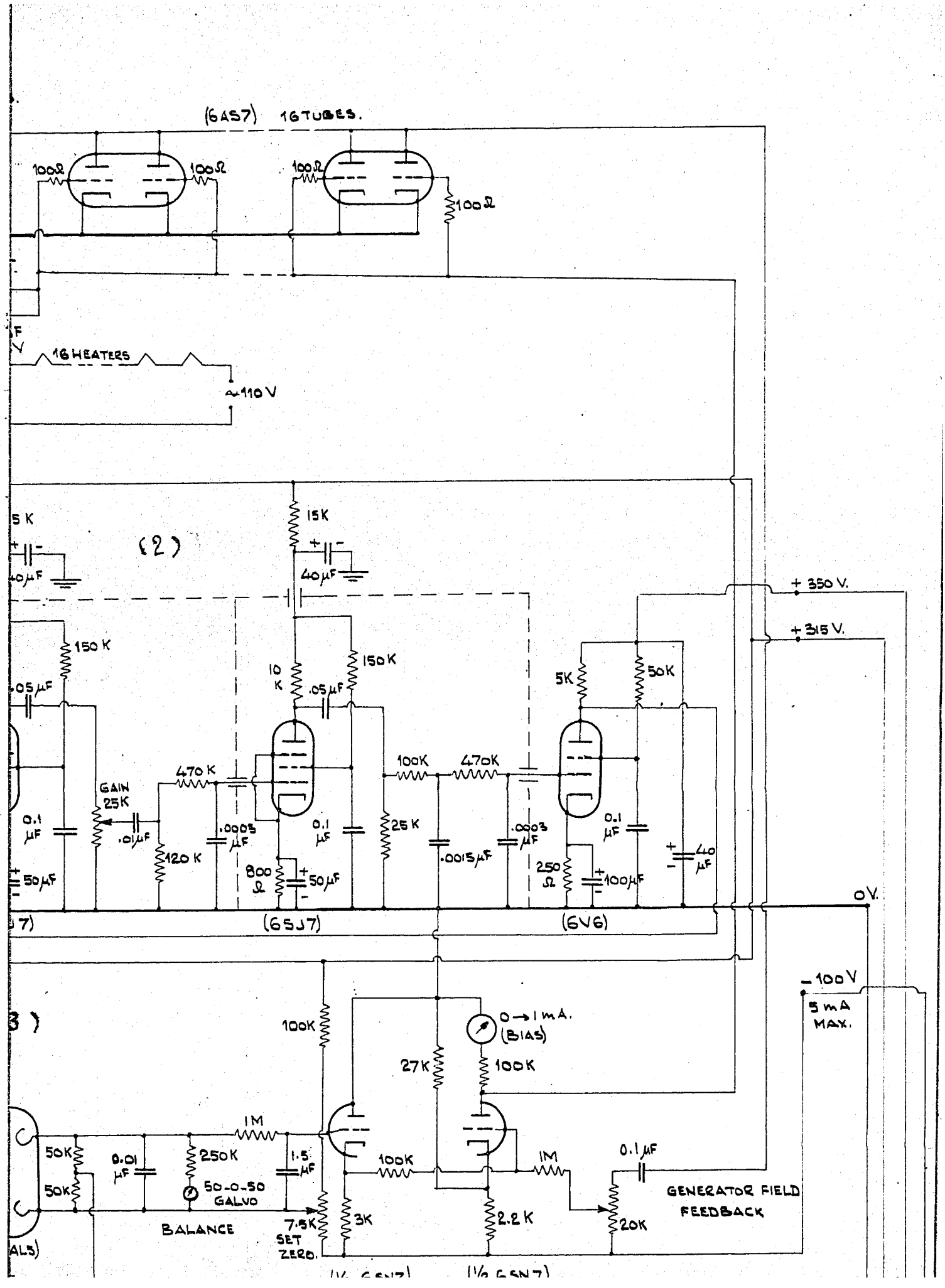
(6AS7) 16 TUBES.
100Ω
100Ω
100Ω
100Ω
16 HEATERS
~110 V
5 K
40μF
(2)
15K
40μF
+ 350 V.
+ 315 V.
150 K
.05μF
10 K
150K
.05μF
5K
50K
470 K
100K
470K
GAIN 25K
0.1 μF
.01μF
120 K
.0003 μF
0.1 μF
25 K
.0015μF
.0003 μF
0.1 μF
50μF
800 Ω
50μF
250 Ω
100μF
40 μF
0V.
7)
(6SJ7)
(6V6)
(3)
100K
0→1 mA. (BIAS)
27K
100K
- 100 V
5 mA MAX.
1M
50K
50K
0.01 μF
250K
50-0-50 GALVO
1.5 μF
100K
1M
0.1μF
GENERATOR FIELD FEEDBACK
BALANCE
7.5K SET ZERO.
3K
2.2 K
20K
ALS)
1/2 6SN7
1/2 6SN7

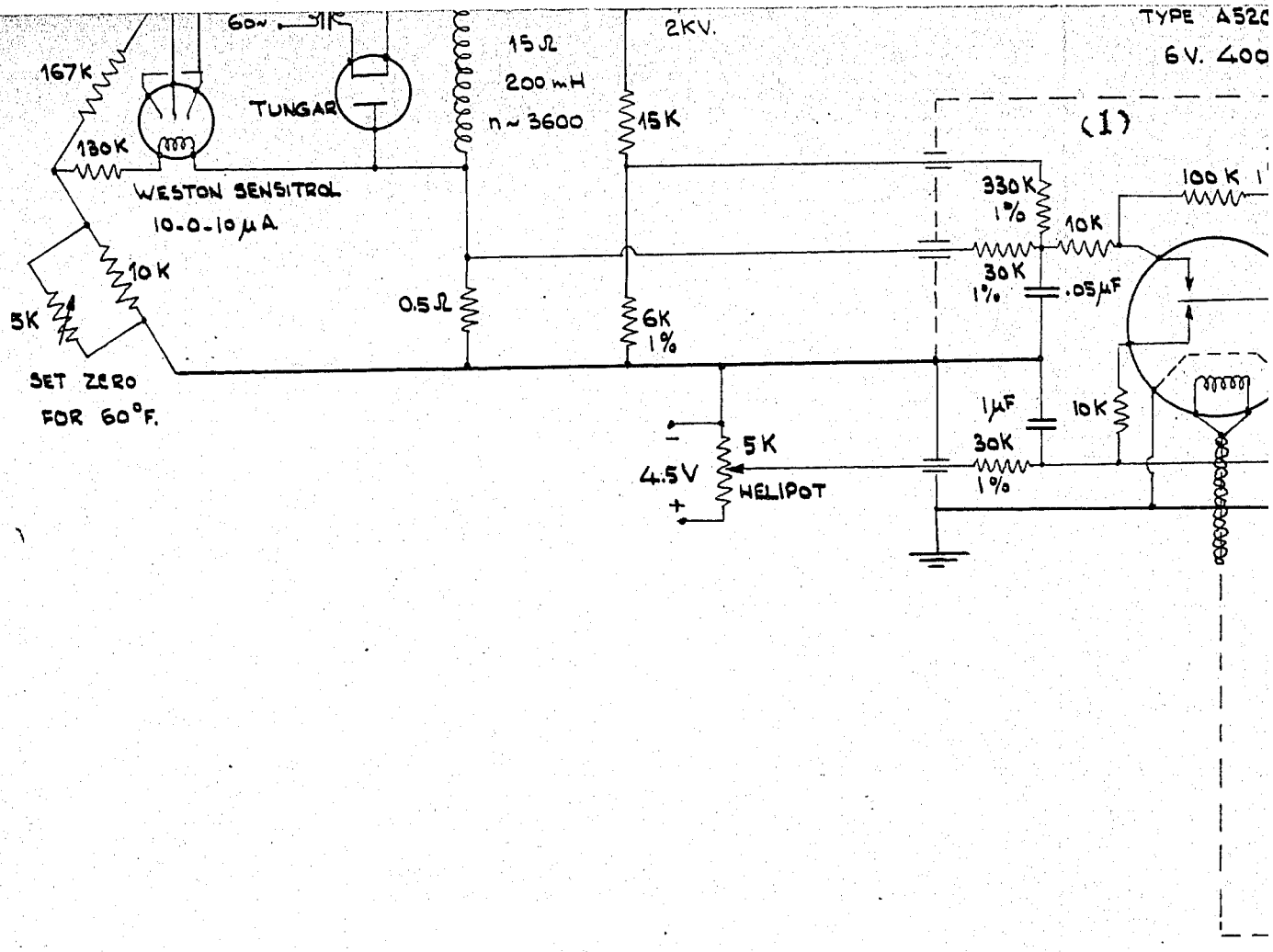

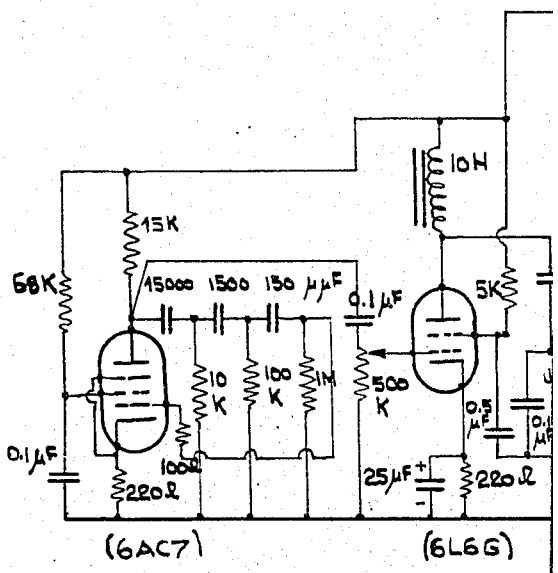

Fig. 2. **BETA SPECTROMETER**

MAGNET STABILIZER.

ORIGINALLY USED FOR THE NEUTRON
LIFE TIME EXPERIMENT.

T_1 : HAMMOND # 333.

T_2: " # 344.

T_3: " # 270.

SEPT. 2/57
dwf.

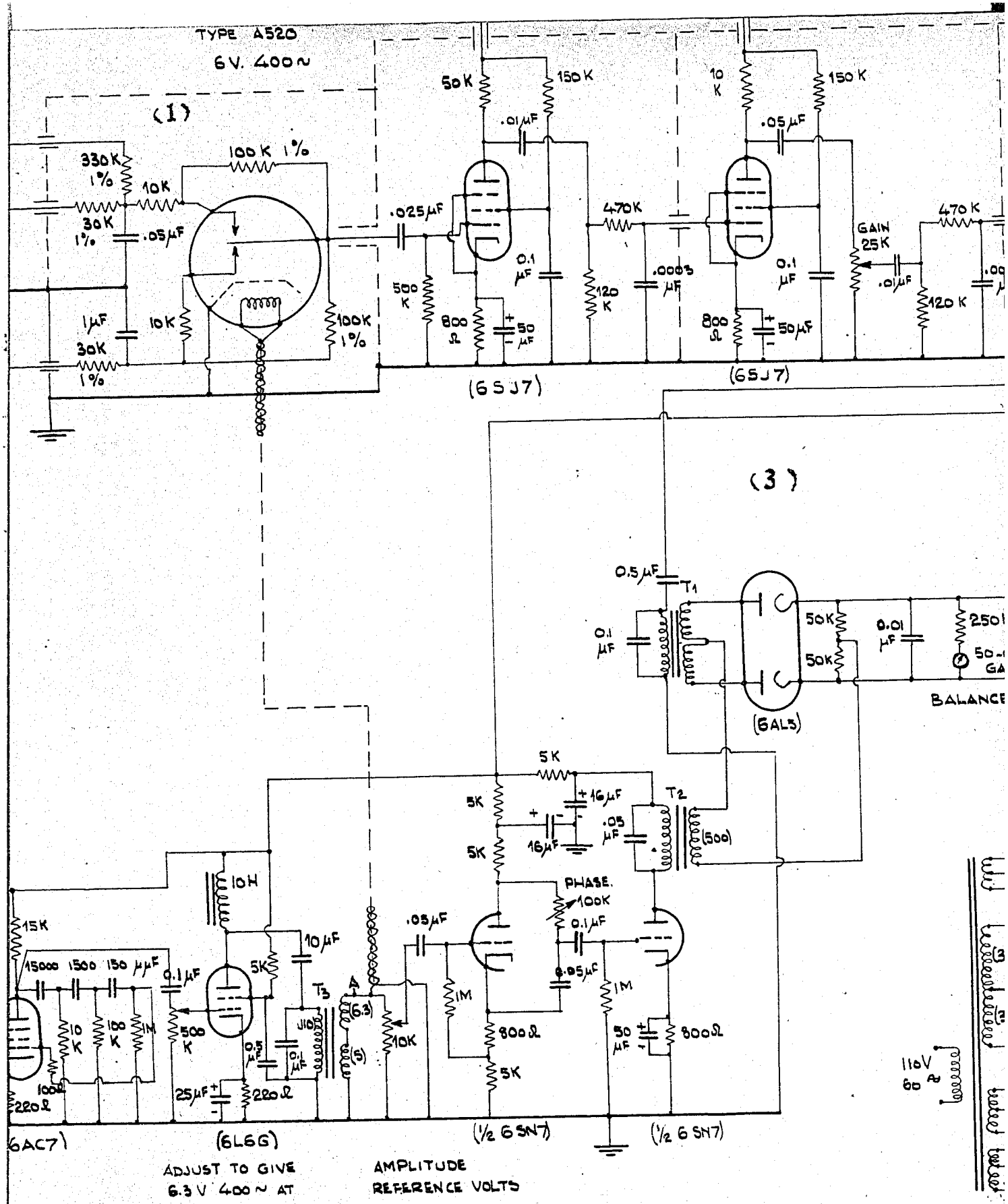
TYPE A520
6V. 400~
(1)
330K 1%
10K
30K 1%
.05μF
100K 1%
1μF
10K
30K 1%
100K 1%
.025μF
50K
150K
.01μF
500K
800Ω
50 μF
0.1 μF
120K
470K
.0003 μF
(6SJ7)
10K
150K
.05μF
0.1 μF
800Ω
50μF
GAIN 25K
.01μF
470K
120K
(6SJ7)
(3)
0.5μF
T1
0.1 μF
50K
50K
0.01 μF
BALANCE
(6AL5)
5K
5K
5K
16μF
16μF
.05 μF
T2
(500)
PHASE. 100K
0.1μF
.05μF
.05μF
1M
1M
800Ω
800Ω
50 μF
5K
10H
15K
15000 1500 150 μF
10K
100K
1M
1000Ω
220Ω
0.1μF
500K
5K
10μF
T3
0.5 μF
.01 μF
25μF
220Ω
A
(6.3)
(5)
10K
(6AC7)
(6L6G)
(½ 6SN7)
(½ 6SN7)
110V 60~
ADJUST TO GIVE 6.3 V 400~ AT A → GROUND
AMPLITUDE REFERENCE VOLTS

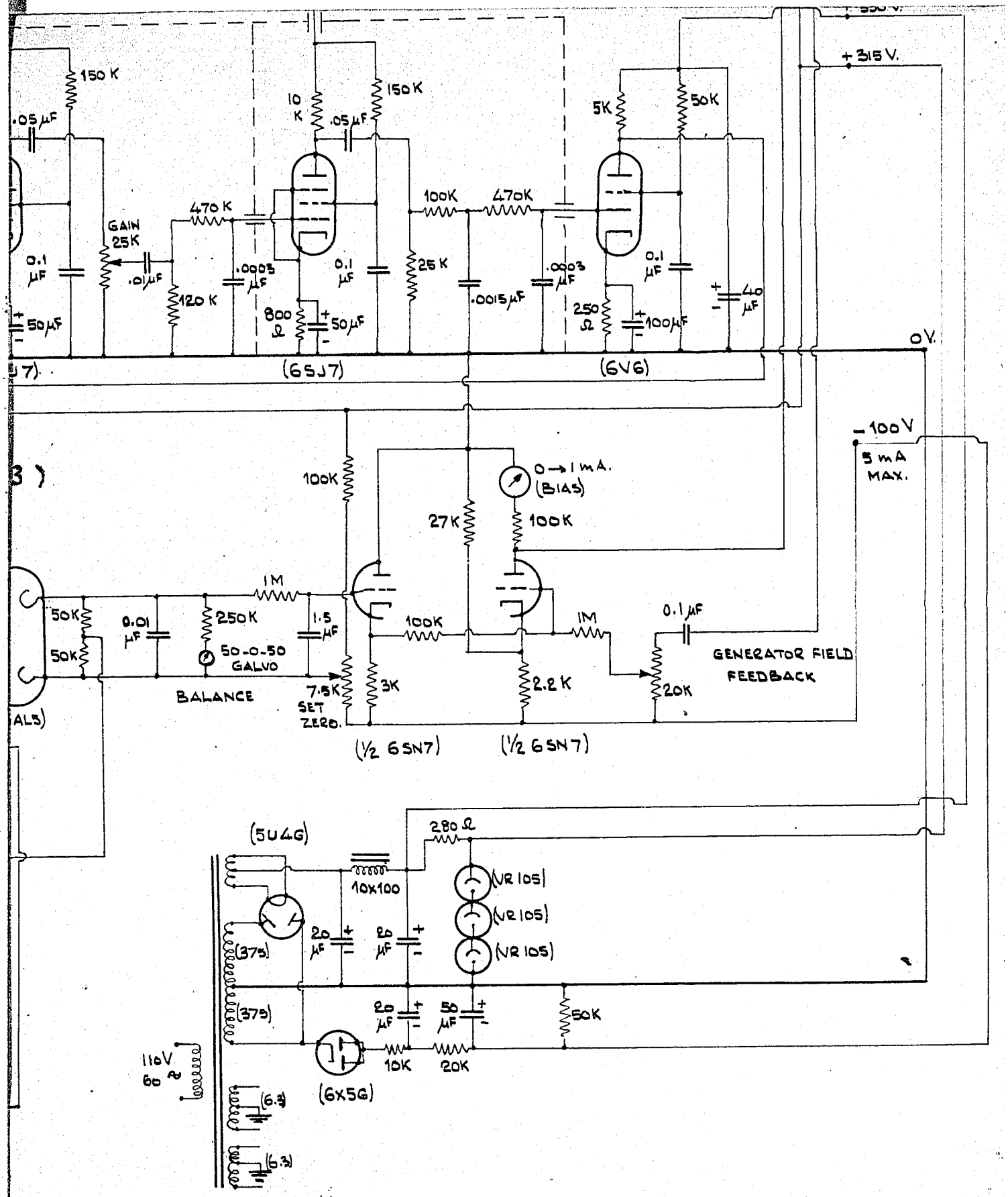
+315 V.
150 K
.05 μF
10 K
150 K
.05 μF
5K
50K
GAIN 25K
470 K
100K
470K
0.1 μF
.01 μF
120 K
.0003 μF
0.1 μF
25 K
.0015 μF
.0003 μF
0.1 μF
40 μF
50 μF
800 Ω
50 μF
250 Ω
100 μF
0 V.
(6SJ7)
(6SJ7)
(6V6)
-100 V
5 mA MAX.
0 → 1 mA. (BIAS)
100K
27K
100K
1M
50K
50K
0.01 μF
250K
1.5 μF
50-0-50 GALVO
BALANCE
7.5K SET ZERO.
100K
1M
0.1 μF
3K
2.2K
20K
GENERATOR FIELD FEEDBACK
(½ 6SN7)
(½ 6SN7)
(5U4G)
280 Ω
10x100
(VR 105)
(VR 105)
(VR 105)
20 μF
20 μF
(375)
(375)
20 μF
50 μF
50K
110V 60 ~
10K
20K
(6X5G)
(6.3)
(6.3)

very small so that I = V/R, (I is the current throughthe magnet coil). The current I, therefore, is controlled by the setting of helipot. Feed back is applied from the voltage across the magnet coil in order to stabilize the system. This voltage leads the current through the coil by approximately 90° in phase so that stabilization is achieved by the "phase advance" method of standard servomechanism theory.

Safety devices are incorporated to protect the magnet, one using the principle of a Wheatstone bridge to protect the magnet against overheating and another using an inverted diode to prevent excessive surge voltages if the connecting leads are accidentally open circuited while carrying a large current.

B. Short Magnetic Lens

In a short magnetic lens type spectrometer, electrons are focussed depending on the "chromatic aberration" properties in much the same way as the optical lens. Deutsch et al (1) and Fretter (2) give the relation between focal length f, source distance u, and image distance v:-

$$\frac{1}{f} = \frac{1}{u} + \frac{1}{v} \qquad (3)$$

which is the same relation as in the optical lens case. In

our case, u = v = 42.2 cm, hence f = 21.1 cm. The focal length actually is varied by varying the current through the coil so that with a given current through the coil only electrons of a certain momentum will be focussed onto the detector. The magnetic field necessary to focus electrons into the counter is proportional to the momentum of the electron; Deutsch et al (1) give the relation

$$f = C\,(p/ni)^2 \tag{4}$$

One can rewrite this

$$ni = \sqrt{\frac{k\,\bar{a}}{f}}\,p \tag{5}$$

where p is the momentum in gauss cm and is given by

$$p = B\rho = mv \times \frac{c}{e} \tag{6}$$

using the eq. (1). C and k are constants depending upon the dimensions of the magnet coil, and $\bar{a}$ is the mean radius of the coil, i.e., $\bar{a} = (a_1 + a_2)/2$; where, a_1 is the inner radius of the coil, and a_2 is the outer radius as shown in Fig. 1.

One can decompose the motion of electrons in the vacuum chamber into 2 components. The axial and the radial components V_z and V_r of the velocity V of electrons of

certain momentum emitted from the source in the vacuum at the angle ϕ with the axis are

$$V_z = V \cos \phi \tag{7}$$

$$V_r = V \sin \phi \tag{8}$$

when the magnet field is off. Now, the magnetic field B parallel to the axis will cause the electrons to travel in circle of radius ρ in the projected plane as shown in Fig. 3. ρ is constant if the field B is constant. Corrections for the non-uniform field B will be made later. Using the eq. (1) and eq. (8) we get

$$F = \frac{e(\vec{V} \times \vec{B})}{c} = \frac{eV \sin\phi B}{c}$$

$$= \frac{eV_r B}{c} = \frac{mV^2_r}{\rho}$$

i.e.
$$\rho = \frac{mV_r c}{eB} \tag{9}$$

Gaston Fisher (3) introduced the idea of time of flight of electron τ sec in the vacuum chamber by which he derived the relation between V_r and V_z

$$\tau = \frac{2\pi\rho}{V_r} = \frac{L}{V_z} \tag{10}$$

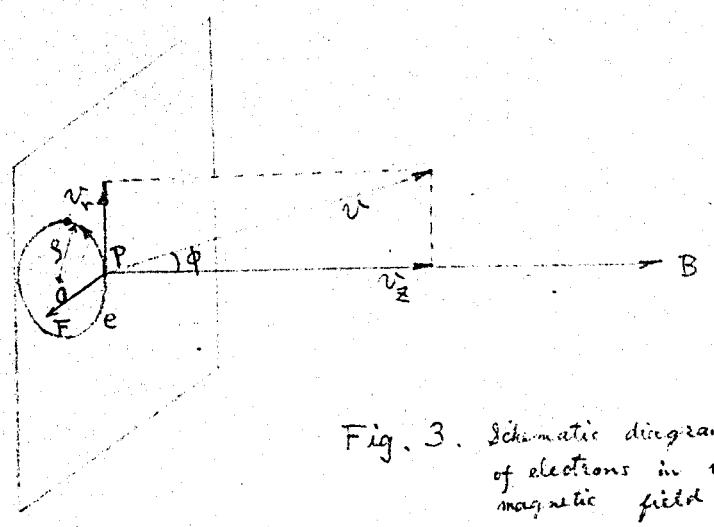

Fig. 3. Schematic diagram of motion of electrons in uniform magnetic field.

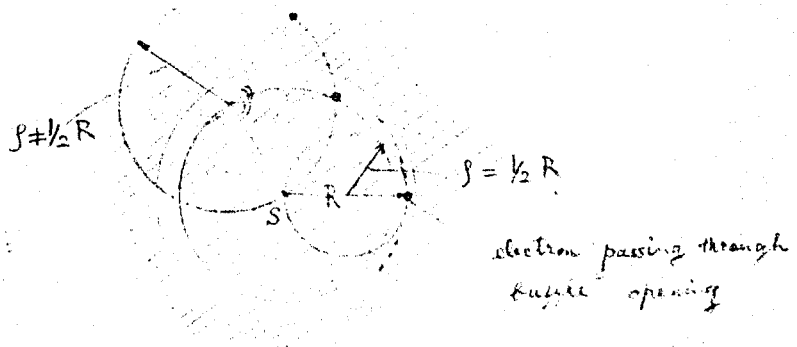

Fig. 4. Electrons passing through baffle opening with different ρ.

where, L = u + v is the length of chamber as shown in Fig. 1. By putting eq. (9) into eq. (10), one can get

$$V_z = \frac{LV_r}{2\pi\rho} = \frac{Le\,B}{2\pi mc} \qquad (11)$$

Now, if R is the radius of the baffle aperture (see Fig. 1,4), the electrons having the radius of curvature ρ which is equal to $\frac{1}{2}R$ will pass the baffle opening and be focussed onto the detector,

$$\text{i.e.} \qquad \rho = \tfrac{1}{2}R \qquad (12)$$

In other words, some of the electrons of curvature ρ which are not equal to $\frac{1}{2}R$ may pass through the baffle gap, but they will not be focussed onto the detector. This is apparent because the angle of rotation of the electrons during the path from the source to the baffle and from the baffle to the image must be the same, since $u = v = \frac{L}{2}$. A sketch of this situation is made in Fig. 4.

Substituting eq. (12) into eq. (9), we get

$$V_z = \frac{ReB}{2mc} \qquad (13)$$

Kinetic energy T of electrons of velocity V in the relativistic expression is

$$T = \frac{1}{2}\,m_0V^2\,(1 + \frac{3}{4}\,\frac{V^2}{c^2} + \ldots\ldots) \qquad (14)$$

where, m_o is the rest mass. Rewriting eq. (14),

$$T = \frac{1}{2} m_o (V_r^2 + V_z^2) \left\{1 + \frac{3}{4} \frac{(V_r^2 + V_z^2)}{c^2} + \ldots\ldots\right\} \quad (15)$$

By substitution for V_r and V_z using eq. (11) and (13),

$$T = \frac{m_o}{2} \left\{ \frac{R^2 e^2 B^2}{4m^2 c^2} + \frac{L^2 e^2 B^2}{4\pi^2 m^2 c^2} \right\} \left\{1 + \frac{3}{4} \frac{1}{c^2} \left(\frac{R^2 e^2 B^2}{4m^2 c^2} + \frac{L^2 e^2 B^2}{4\pi^2 m^2 c^2} \right) + \ldots\right\}$$

$$= \frac{m_o e^2 B^2}{8m^2 c^2} \left\{ R^2 + \frac{L^2}{\pi^2} \right\} \left\{1 + \frac{3e^2 B^2}{16m^2 c^4} \left(R^2 + \frac{L^2}{\pi^2} \right) + \ldots\ldots\ldots\ldots\right\}$$

$$= \frac{(1-\beta^2) e^2 B^2}{8m_o c^2} \left(R^2 + \frac{L^2}{\pi^2} \right) \left\{1 + \frac{3e^2 B^2}{16 m_o^2 c^4} (1-\beta^2) \left(R^2 + \frac{L^2}{\pi^2} \right) + \ldots\ldots\right\} \quad (16)$$

where,

$$m = \frac{m_o}{(1-\beta^2)^{\frac{1}{2}}} \quad (17)$$

We can say from eq. (16) that the kinetic energy T of electrons focussed onto the detector of fixed geometry will depend only upon the strength of magnetic field.

Now, the radius of curvature ρ actually is not constant in the case of a short magnetic lens spectrometer since magnetic field strength is varying with Z. This can easily be seen from eq. (9). We can get the rotation of electrons with respect to the center O of radius of curvature $\rho(B)$ by taking the small angle of rotation of electron $d\theta$ as shown in Fig. 5. In this case the point O itself is

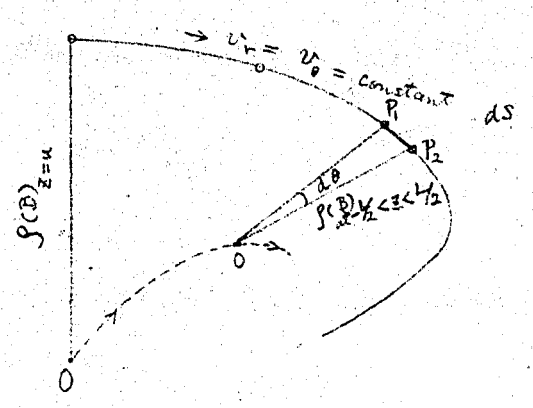

Fig. 5. Rotation of electron around the point O.

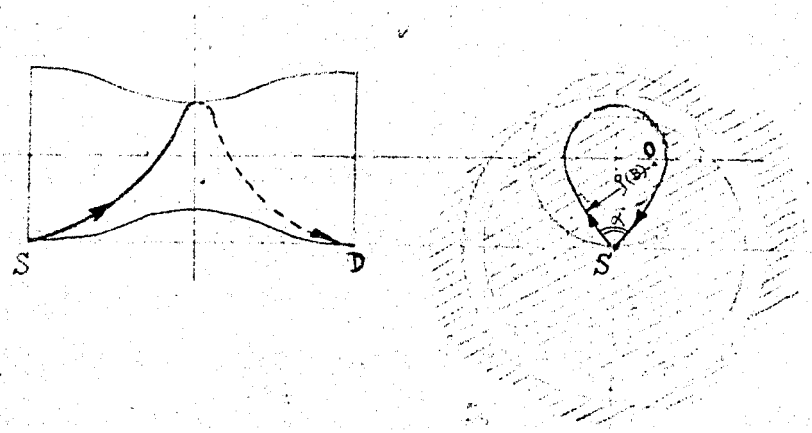

Fig. 6. Electron trajectory along the surface of the concave drum.

moving as shown with the dotted line in Fig. 5.

$$\text{i.e.} \qquad d\theta = \frac{V_\theta}{\rho(B)}\, dt \qquad (18)$$

where, V_θ is the velocity of electrons along the circular line and is equal to V_z.

$$\therefore \qquad d\theta = \frac{V_z}{\rho(B)}\, dt \qquad (19)$$

By substitution for $\rho(B)$ using eq. (9), and integrating it, we get for rotation of 180° around point O;

$$\theta = \int_0^{\pi} d\theta = \pi = \int_0^{\tau/2} \frac{e}{mc} B\, dt \qquad (20)$$

Let $V_z t = Z$, then $V_z dt = dZ$,

$$\therefore \qquad \theta = \frac{e}{2mc} \int_0^{L} \frac{B}{V_z}\, dZ = \frac{1}{2mcV\cos\beta} \int_0^{L} B\, dZ \qquad (21)$$

Since B in our case has a Gaussian distribution, we can estimate the rotation θ at any distance Z by knowing the B distribution curve and numerically integrating it. The electron trajectories can now be represented graphically something like in Fig. 6. Siegbahn (4) and Deutsch et al, give the rotation of electron α around the axial line of the magnet represented by the point S in Fig. 6.

$$\text{i.e.} \quad \alpha = \frac{\pi K}{\sqrt{K^2+1}} \tag{22}$$

$$\text{where } K = \frac{B_0(0)\, b}{2B\rho} \tag{23}$$

and b is the half width of field curve.

Deutsch et al (1) developed the formula for the magnetic field on the axis B_o

$$B_o = 2\pi ni/160(a_2-a_1) \times \left[(Z+L/2)\ln\left\{\left(a_2+\left[a_2^2+(Z+L/2)^2\right]^{\frac{1}{2}}\right)\Big/\left(a_1+\left[a_1^2+(Z+L/2)^2\right]^{\frac{1}{2}}\right)\right\} - (Z-L/2)\ln\left\{\left(a_2+\left[a_2^2+(Z-L/2)^2\right]^{\frac{1}{2}}\right)\Big/\left(a_1+\left[a_1^2+(Z-L/2)^2\right]^{\frac{1}{2}}\right)\right\}\right] \tag{24}$$

They also presented the equations for motion of electrons under the influence of the magnetic field,

$$\begin{aligned} \frac{d}{dt} m\dot{z} &= -\frac{e^2}{mc^2} A \frac{\delta A}{\delta z}, \\ \frac{d}{dt} m\dot{r} &= -\frac{e^2}{mc^2} A \frac{\delta A}{\delta r}, \\ mr\dot{\theta} &= -\frac{e}{c} A, \end{aligned} \tag{25}$$

where, A is the vector potential of magnetic field, and dot indicates the derivative with respect to time t. By applying

boundary conditions and integrating these eq. (25), and by working out some approximation method they derived the correlations

$$(ni/p_o)^2_{r\to o} = 3.07$$

$$(ni/p_o)^2_{r = 7.3cm} = 6.72 \qquad (26)$$

where, p_o is the momentum of the focussed electron. We can rewrite the eq. (26)

$$p_o(r\to o) = 0.352ni$$

$$p_o(r=7.3cm) = 0.386ni \qquad (27)$$

This means that for any values of the magnet current, electrons focussed through the outermost part of the baffle have a larger momentum than the electrons focussed passing close to the axial line. In order to minimize the effect of spherical aberration, one has to use the baffle system.

To find the theoretical values of resolution at half height $R_{\frac{1}{2}}$, we can make use of the relation presented by Siegbahn (4).

$$R_{\frac{1}{2}} = \frac{S+W}{4R} \qquad (28)$$

where, S and W are the radii of the source and scintillation crystal respectively. R in this case represents the inner radius of the baffle opening.

One can derive equ. (28) as follows: i.e., by expanding the axial component of the trajectory of an electron into the plane, one gets the triangular relation as shown in Fig. 6-A.

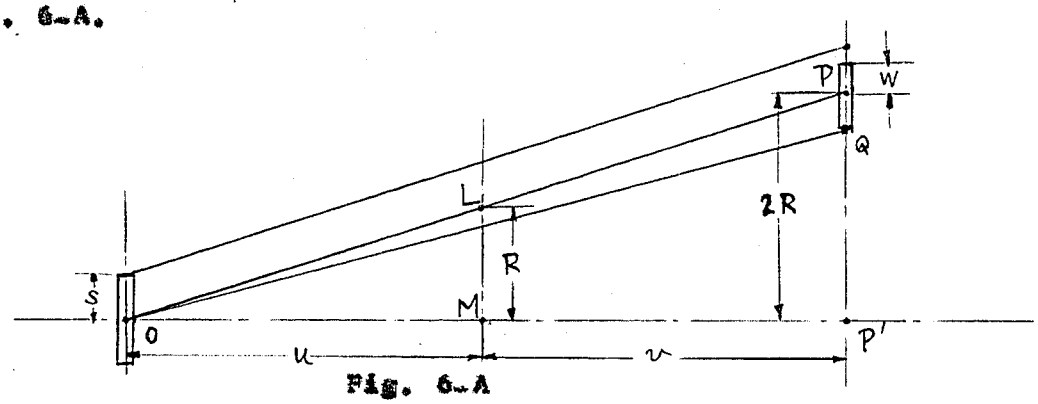

Fig. 6-A

Geometry of source and detector expanded into the plane.

It is apparent from eq. (6), eq. (12) and Fig. 4, that R is proportional to momentum of an electron p, if B is fixed. Hence, p is proportional to PP' = 2R, (since u = v in this case). Hence, spread of momentum Δp_1 due to certain width W of the detector is related by

$$\frac{\Delta p_1}{p} = \frac{W}{2R}$$

Now, spread of momentum Δp_2 due to certain width S of the source is superimposed onto Δp_1:

i.e. $$\frac{\Delta p_2}{p} \doteqdot \frac{S}{2R}$$

Hence, resolution at base R_o is roughly expressed by

$$R_o = \frac{\Delta p_o}{p} = \frac{\Delta p_1 + \Delta p_2}{p} \doteqdot \frac{S + W}{2R}$$

Assuming that the width at half height is approximately $\frac{1}{2}$ of the base width, and neglecting the effect of the spherical aberration,

one gets the expression for $R_{\frac{1}{2}}$:

$$R_{\frac{1}{2}} = \frac{\Delta P}{P} \doteq \frac{1}{2} \times \frac{\Delta P_o}{P} = \frac{1}{2} \times \frac{S + W}{2R} = \frac{S + W}{4R}.$$

Approximate transmission T of the specific set up is found using the relation

$$T = \frac{2\pi R \Delta R}{4\pi u^2} = \frac{R\Delta R}{2u^2} \qquad (29)$$

where, ΔR is the width of the baffle opening.

C. Degaussing Coils

According to the information of the Dominion Observatory, the earth magnetic field in Ottawa is as follows.

(i) Horizontal component = 14650 γ and changing with the rate + 10 γ/year,

(ii) Vertical component = 57680 γ and changing with the rate -20 γ/year.

(iii) Total field = 59700 γ and changing with the rate -20 γ/year.

where, 100,000 γ = 1 gauss.

These are the values at the beginning of 1955.

For our experiment, the effect of the horizontal component can be minimized by arranging the axis of the magnet coil exactly to the magnetic N-S direction, but the vertical component should be compensated in some ways. For this purpose, we can apply the principle of the Helmholtz arrangement.

L.B. Loeb (5) gives the expression for the field produced by a small element ds of the circular coil at a point P distant x cm from the plane of the coil along the normal to the coil at its center as shown in Fig. 7,

$$dB = \frac{ids}{L^2} \tag{30}$$

where, i is the current through the coil. The element of the field in which we are interested is the component parallel to the axis of the coil and is

$$dB_1 = dB \sin \theta \tag{31}$$

If the number of turns in the coil be n, then,

$$dB_1 = \frac{ni\, d\varphi \sin \theta}{L^2} \tag{32}$$

where,

$$L = \frac{r}{\sin \theta}, \text{ and } L^2 = r^2 + x^2$$

Integrating the eq. (32), L. Loeb gets:

$$B_1 = \int_0^{B_1} dB_1 = \frac{nir}{(r^2+x^2)^{3/2}} \int_0^{2\pi r} ds = \frac{2\pi nir^2}{(r^2+x^2)^{3/2}} \tag{33}$$

It is seen from eq. (33) that B_1 decreases as x increases. The rate of change of B_1 with x is $\frac{dB_1}{dx}$,

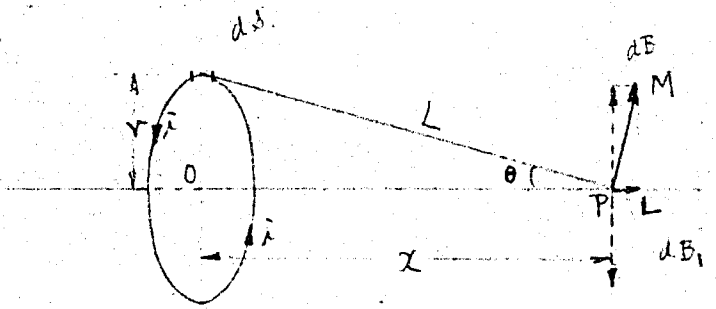

Fig. 7. Field due to circular coil.

$$\text{i.e.} \qquad \frac{dB_1}{dx} = \frac{-6nir^2x}{(r^2+x^2)^{5/2}} \begin{cases} < 0 \text{ when } x > 0 \\ > 0 \text{ when } x < 0 \end{cases} \qquad (34)$$

Now, by taking the second derivatives of B_1 with respect to x and setting it equal to zero, we find the point where the rate of change of B_1 with x becomes constant.

$$\text{i.e.} \qquad \frac{d^2B_1}{dx^2} = \frac{-6nir^2(r^2-4x^2)}{(r^2+x^2)^{7/2}} = 0 \qquad (35)$$

$$\therefore \qquad x = \pm \frac{r}{2} \qquad (36)$$

Hence, if we have two identical coils placed on the same axis each $\frac{r}{2}$ distance apart from a point P, the field B_1 from the two coils is quite constant for a considerable range. These arrangements are called "Helmholtz coils". Then we have the relation

$$B_1 = \frac{4 \ nir^2}{(r^2+\frac{r^2}{4})^{3/2}} = \frac{2.86 \ ni}{r} \qquad (37)$$

Using the gauss cm and ampere units, Bechman (6) gives the expression

$$B = \frac{0.286\pi nI}{r} \qquad (38)$$

D. Vacuum Systems

It is necessary for the magnetic beta ray spectroscopy to keep a good vacuum in the chamber to prevent the electrons from the interactions with gas molecules. Interactions of electrons with the gas molecules knock the electron out of the trajectories causing the error to our experimental results.

These interactions include ionization of gas molecules, forward and backward scattering by gas nuclei, scattering by atomic electrons, and Bremsstrahlung. In the energy regions we are concerned, however, the effect of Bremsstrahlung can be neglected. R.D. Evans (6) tabulated the approximate cross sections per atom of air for 0.1 MeV electrons:

Ionization	1700 barns
Nuclear elastic backward scattering	130 barns
Electronic scattering	230 barns
Bremsstrahlung	negligible

Modifying the nuclear cross sections, we get total cross section for interaction between electron and the air molecules, $\sigma_{total/molecule} = (1700+130+230) \times 2$

$= 4160$ barns (39)

We use the following relation to get approximate macroscopic cross section Σ of air for electrons.

$$\Sigma = \frac{0.6\,\sigma_{tot}\,d}{M} \qquad (40)$$

where, d is the density of air which depends upon pressure and temperature. The value of d at atmospheric pressure and room temperature is

$$d = 0.00121 \quad g/cm^3,$$

and at pressure p mmHg,

$$d(p) = 0.00121 \times \frac{p}{760} \qquad (41)$$

M is the molecular weight of the air and is approximately equal to 29.0

Hence, mean free path of air at various pressure $\lambda(p)$ is given by the relation,

$$\lambda(p) = \frac{1}{\Sigma} = \frac{M}{0.6\,\sigma_{tot}\,d} \times \frac{760}{p}$$

$$= \frac{29.0}{0.6 \times 4160 \times 0.00121} \times \frac{760}{p}$$

$$= \frac{7.31 \times 10^3}{p} \qquad (42)$$

This will give an absolute upper limit to the permissible pressure since in practice we have to take into account the forward scattering which is much bigger than the backward scattering. R.D. Evans (7) gives

$$\sigma(\geq\theta) = \frac{\pi}{4} b^2 \cot^2\frac{\theta}{2} \qquad (43)$$

where, $\sigma(\geq\theta)$ is the cross section for scattering through an angle θ or greater, and b is the distance of the closest possible approach of particles in Rutherford scattering.

An alternative lower limit estimate can be made from the data of Bachman (8) who describes that the mean free path of slow electrons moving through a gas is greater than that of a molecule of the gas by a factor of $4\sqrt{2}$. He tabulates the mean free path of nitrogen at various pressures;

760 mmHg ..... 6.7×10^{-6} cm

1 mmHg ..... 5.1×10^{-3} cm

10^{-3} mmHg ..... 5.1 cm

10^{-5} mmHg ..... 500 cm

Hence at 1 micron of nitrogen atmosphere, mean free path $\lambda(p)$ is

$$\lambda(p) = 5.1 \times 4\sqrt{2} = 28.8 \text{ cm}$$

This can be interpreted in air without too much error. So, for our set up, in which electrons travel along the vacuum chamber of about 85 cm long, a lower limit to the required pressure would be $\sim$0.3 microns. This will be a lower limit since our electrons are of higher energy and, therefore, with longer mean free paths than those considered by Bachman.

A Pirani gauge and an ionization gauge have been used in our set up to measure the degree of vacuum. A Pirani gauge is provided for the comparatively low vacuum region (10^{-1} to 10^{-4} mmHg) and an ionization gauge for the high vacuum region (10^{-3} to 10^{-7} mmHg).

The Pirani gauge makes use of the principle of Wheatstone bridge circuit and the cooling effect of gas molecules. The result is observed as the variation in resistance of a very fine filament heated by passing a known amount of current through it. A simplified circuit diagram of the Pirani gauge used in our experiment is shown in Fig. 8. The Gauge G_1 is the reference gauge permanently sealed off at high vacuum, while G_2 is connected with the vacuum chamber so that the presence of gas molecules effects the temperature of the filament with a resulting variation in resistance of the filament. This change in resistance is compared with the resistance of the reference gauge filament in a bridge circuit. In order to get the high sensitivity, the temperature coefficient of resistance of

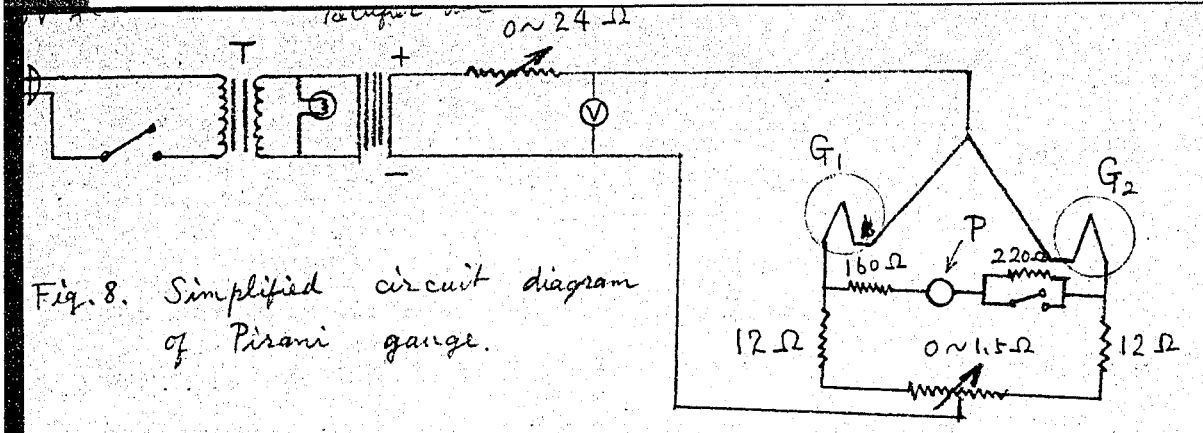

Fig. 8. Simplified circuit diagram of Pirani gauge.

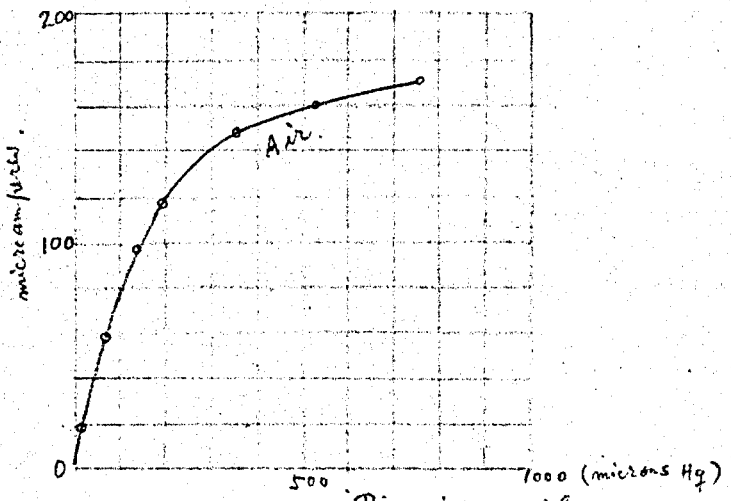

Fig. 9. Response curve for Pirani gauge.

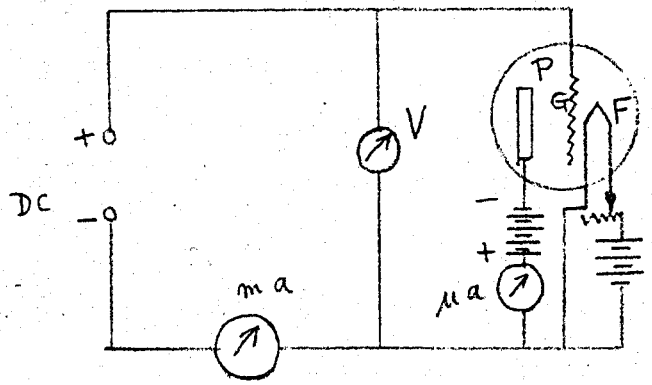

Fig. 10. Simplified circuit of ionization gauge.

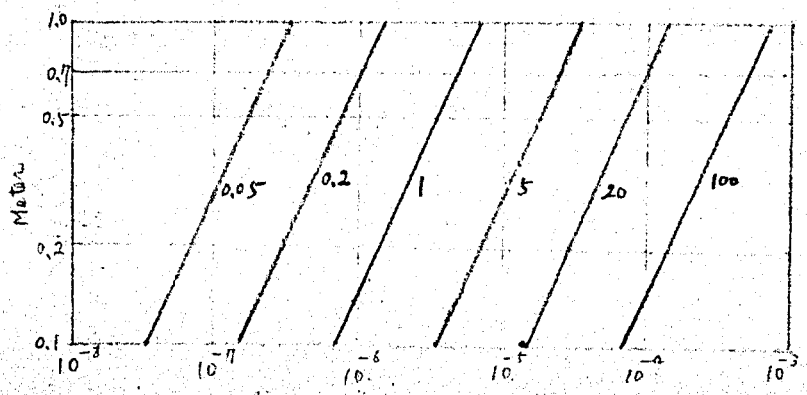

Fig. 11 Ionization gauge characteristic

the filament must be very large. Distillation Products Inc., gives the curve for response of the galvanometer to the pressure in the system. This is reproduced in Fig. 9. One can see from this curve that the response is not linear with the pressure, and that the gauge is not sensitive in the range of the lower degree of vacuum.

The ionization gauge is a triode mounted in a glass envelope. The grid structure is operated positive with respect to the filament by 187 volts in our gauge. The collecting plate is run negative to the filament by 13 volts. Fig. 10 shows the circuit diagram of our ionization gauge in a simplified form. Electrons leaving the filament are accelerated toward the grid which is positive to the filament, and some of the electrons are collected on the grid; some of them, however, pass through grid into the region between the grid and the collecting plate. These electrons cause ionization of the gas molecules; the positive ions so formed are then collected by the plate and measured with a microammeter. The number of positive ions formed is a function of the gas pressure of the system. If the gas pressure is too high, the multiple ionization phenomenon will occur, causing considerable error in the readings. But below about one micron the characteristics is a straight

line as shown in Fig. 11. The number of electrons emitted from the filament must be very stable in order to operate the gauge with a high accuracy. A special stabilizing circuit is therefore used which maintains the grid current constant.

E. Scintillation Counter

Various method to detect the focussed electrons are available among which the scintillation counter method is one of the most useful. This method has been applied in our experimental set up, and all the counting instruments except scaler have been built by ourselves. Details of these electronic circuits are described in the thesis of Hans De Vries (17) who has been the co-worker during the whole experiments.

An anthracene crystal is used as a scintillator, and the following relation is used to find the thickness of the crystal.

$$R = 0.11\left(\sqrt{1 + 22.4\, E_o^2} - 1\right)$$

$$0 < E_o < 3\text{MeV}. \qquad (44)$$

where, R is the range of the electrons, in g/cm^2, and E_o is the maximum energy of the beta spectrum. This empirical relation is derived by Flammersfeld (9). Actually various

other expressions for R and E_o have been given by a number of authors, but they turned out to be about the same results. Thickness of ~2.0 mm is found to be the best to stop ~80% of the electrons of 500~1000 KeV energy.

The examples of the crystal thickness calculations are given below:

(i) For higher energy component of Cs^{137}.

$$E_o = 1.2 \text{ MeV};$$

$$\therefore \quad R = 0.11 \left\{ \sqrt{1 + 22.4 \times 1.2^2} - 1 \right\}$$

$$= 0.526 \text{ g/cm}^2$$

and $\rho = 1.2$ g/cc.

$$\therefore \quad \frac{0.526}{1.2} = 4.38 \text{ mm}$$

(ii) For lower energy component of Cs^{137}.

$$E_o = 0.51 \text{ MeV};$$

$$\therefore \quad R = 0.11 \left\{ \sqrt{1 + 22.4 \times 0.51^2} - 1 \right\}$$

$$= 0.287 \text{ g/cm}^2$$

$$\therefore \quad \frac{0.287}{1.2} = 2.39 \text{ mm}$$

While, 92% of the total disintegration occurs with the maximum energy of 0.51 MeV. Hence, ~2.0 mm thick anthracene

will stop roughly 80% of the electrons emitted from the Cs^{137} source. About 20% of the electrons which are not completely stopped are still dissipated in the anthracene causing smaller pulses.

Anthracene ($C_{14}H_{10}$ or $C_6H_4(CH)_2C_6H_4$) is a product of the destructive distillation of coal and presents in coal-tar to the extent of 0.25 to 0.5 per cent. According to Birks (10), anthracene produces a light flash of $(2.7\pm0.5)\times10^{-8}$ sec. time constant and 4470Å wavelength when electrons strike it. The photomultiplier response is maximum in the range of 4000 ± 500 Å if Sb-Cs alloy is used as a photocathode (11). Anthracene is masked to lucite light pipe and photomultiplier tube is magnetically shielded. The maker recommends to operate 1P21 with the voltage below 1,000 volts to get maximum signal-to-noise ratio.

The preamplifier is mounted directly adjacent to the photomultiplier tube in order to keep its input capacity low, and to gain, thereby, the maximum voltage for a given charge flowing to the anode of the multiplier. The circuit diagram of our preamplifier is shown in Fig. 12.

F. Decay Spectrum of Cs^{137}

5μc of Cs^{137} source deposited on the surface of thin aluminum foil with the effective diameter of 1.2 mm

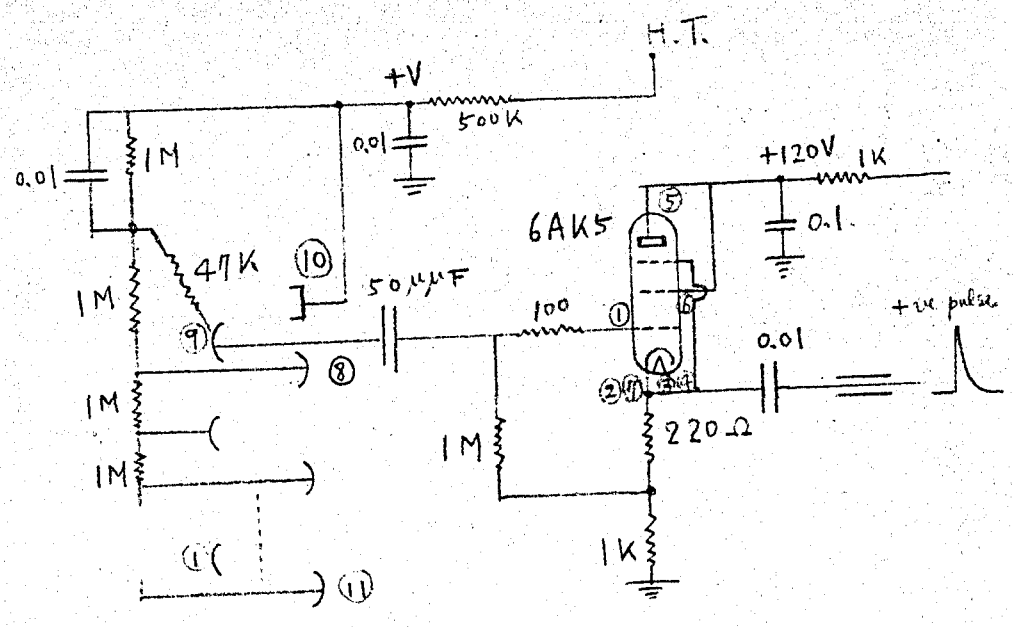

Fig. 12. Photomultiplier and preamplifier circuit.

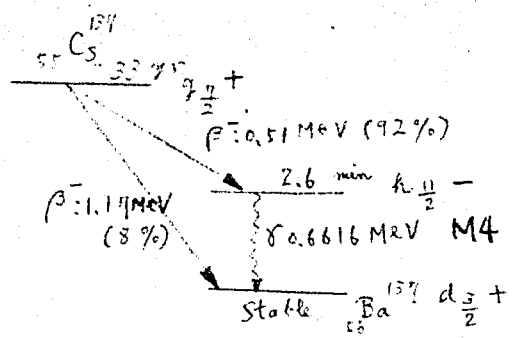

Fig. 13. Decay scheme of Cs^{137}.

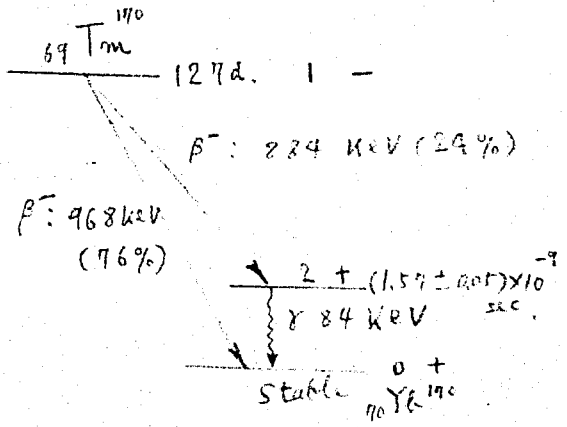

Fig. 14. Decay scheme of Tm^{170}.

was used in our experiment. It is known that the disintegration scheme of Cs^{137} is like that shown in Fig. 13[12] There are two modes of decay in Cs^{137} disintegration. The high-energy beta transition occurs in only 8 per cent of the disintegrations. Hence, in our calibration of the spectrometer, this component is neglected. R.D. Evans gives 510 KeV for the maximum energy of the low-energy beta transition component (92%), and he writes that the shape of the spectrum corresponds to the first forbidden beta decay. According to Evans, the energy of gamma rays from the excited states of Ba^{137} is 661.6 KeV. K edge and average L edge of Ba^{137} is given to be 37.4 KeV and 5.6 KeV, respectively. Evans gives $\alpha_K = 0.08$.

G. Decay Spectrum of Tm^{170}.

2μc of Tm^{170} source deposited on the surface of thin aluminum foil with the effective diameter of 1.2 mm also is used in our calibration.

R.L. Graham, I.L. Wolfson, and R.E. Bell (13) investigated the disintegration of Tm^{170}, and found that 127 day Tm^{170} has two components, one of maximum energy 968 ± 4 KeV (76%) proceeding to the ground state of Yb^{170} and one of maximum energy 884 ± KeV (24%) to an excited state in Yb^{170} followed by emission of a gamma ray or conversion electron to the ground state. Energy of gamma

rays, they found, is 84.1 ± 0.1 KeV, and half-life is $(1.37 \pm 0.05) \times 10^{-9}$ sec. R.L. Graham et al, present the conversion coefficient $\alpha_K = 1.60 \pm 0.15$, $\alpha_L = 4.1 \pm 0.5$. $\alpha_M = 1.2 \pm 0.2$. They used 6 μc, 2 mm diameter source, and examined the spectrum close to the end point with 1.25% resolution spectrometer. They corrected the results for both background and spectrometer resolution. Fig. 14 is the disintegration scheme of Tm^{170} proposed by R.L. Graham et al. In the Fermi-Kurie plot worked out by R.L. Graham et al., two components are separated by extrapolation, assuming that the lower energy component has an allowed shape. They also give the relative intensities of internal conversion groups, by method of comparison of line areas: K/L = 0.36 ± 0.04, K/(L+M) = 0.28 ± 0.03 and L/M = 3.6 ± 0.05.

H. Fermi-Kurie Plot

The method of plotting the spectrum in straight line by correcting for statistical distribution of electron energies, and for electrostatic forces between nucleus and electrons is called "Fermi-Kurie plot". This method is widely used in the study of beta ray spectrum to find the end point. Mr. J.M. Robson gives the equation for number of electrons observed per unit time per unit momentum interval n(p) in his lecture.

$$n(p) = \frac{64\pi^4 m_0^5 c^4 g^2}{h^7} |M|^2 F(Z,p) p^2 (E_0 - E)^2 \quad (45)$$

g is the fundamental constant representing the strength of the beta decay interaction, F(Z,p) is a factor to take into account the electrostatic forces between ejected beta rays and nucleus, and matrix element $|M|^2$ involves wave function of the initial state and the final state of nucleus. This $|M|^2$ is a scalar quantity and is of the order of unity in the allowed beta transitions. For allowed spectrum eq. (45) can be written,

$$n(p) = \text{const.} \times F \times p^2 (T_0 - T)^2,$$

$$\frac{n(p)}{Fp^2} = K_1 (T_0 - T)^2,$$

$$\therefore \quad \sqrt{n(p)/Fp^2} = k_2 (T_0 - T) \quad (46)$$

This relation can be plotted in a straight line. By taking the momentum in mc unit, and kinetic energy of electrons in mc^2 unit, one gets,

$$N(\eta)/\eta^2 (\epsilon_0 - \epsilon)^2 \quad F(Z,\eta) = k \quad (47)$$

where, $\eta = p/mc$, $\epsilon = E/mc^2$, and $\epsilon_0 = E_0/mc^2$. $(\epsilon_0 - \epsilon)$ in eq. (47) is equivalent to $(T_0 - T)$, since $(E_0 - E)$

$= (T_0 + m_0c^2 - T - m_0c^2) = T_0 - T$. Eq. (47) can be rewritten,

$$\sqrt{N(\eta)/\eta^2}\ F(Z,\eta) = k(\epsilon_0 - \epsilon) \qquad (48)$$

The factor $F(Z,\eta)$ for the electrostatic force has been worked out extensively using the relation given in the U.S. National Bureau of Standard Publication AMS13(14);

$$f(Z,\eta) = \eta^2\ F(Z,\eta) = \eta^{2+2S}\, e^{\pm\pi\delta} \left|\Gamma(1+S+i\delta)\right|^2 \qquad (49)$$

where, $S = \sqrt{1-Z^2/137^2} - 1$

and, $\delta = Z\sqrt{1+\eta^2}/137\eta$

The values of $f(Z,\eta)$ is tabulated in the N.B.S. publication AMS13 for all values of Z and for $\eta \leqq 7$. This table has been used in plotting the Fermi-Kurie plot from our experimental results.

Now, if the transition is forbidden, there is (i) a change in angular momentum of $\Delta l = 1$, and hence a parity change or (ii) a change in angular momentum of $\Delta l = 2$, and no parity change as in case of Cs^{137} beta decay. In these cases, the angular momentum will be taken away by the electron and/or neutrino, and one need some correction to get the straight line in the F-K plot. i.e., in the forbidden spectra, Fermi-Kurie plots are made using the relation given by

$$\sqrt{N(\eta)/C\,\eta^2\,F(Z,\eta)} = k\,(\epsilon_0 - \epsilon) \qquad (50)$$

where, C is called the forbidden factor. L.M. Langer and H.C. Price (15) applies

$$C \sim c \sim 3(\epsilon^2 - 1)^2 + 3(\epsilon_0 - \epsilon)^4 + 10(\epsilon^2 - 1)(\epsilon_0 - \epsilon)^2 \qquad (51)$$

and,

$$C \sim a \sim (\epsilon^2 - 1) + (\epsilon_0 - \epsilon)^2 \qquad (52)$$

in their investigation of Cs^{137} spectrum. Eq. (52) refers to 510 KeV transition of Cs^{137}, and eq. (51) refers to 1.17 MeV transition of Cs^{137}.

CHAPTER IV

EXPERIMENTAL DETAILS

A. Starting Situation

The magnet, vacuum chamber, counter rack, oscilloscopes, DC generator, current stabiliser rack, Pirani and ionization gauge unit, scaler, H.T. supply unit, vacuum pumps, beta ray sources, anthracene crystal, fish eye, photomultiplier, wire, batteries, cooling water supply, and all the electronic circuit parts were provided to start with.

The table for spectrometer, degaussing coil systems, vacuum chamber end-plate, source holder, scintillation counter head, single channel pulse height analyzer and pulse generator, were left to be designed and built by ourselves. The magnet current stabilizer circuit, vacuum pumps and vacuum gauges had to be checked and adjusted.

The space available for our experiment was 230 feet by 190 feet including the surrounded tables on which most of the designing and building works have been carried out. The floor was finished with satisfactorily smooth and flat concrete surface without using iron. The horizontal level of the magnetic spectrometer, therefore, was easily obtained. The wooden table for the spectrometer was designed by myself and made outside. Since the table

has to stand for about 900 pounds of weight without causing any serious strain for a long time, plywood of 2 inch thickness was used as a table plate. A framework of wood to holt the degaussing coils was attached onto the table. Since our building fortunately does not contain too much iron, we assumed that the earth magnetic field was not distorted and was quite uniform throughout the room. Besides, great care has been taken to set up the spectrometer in order not to disturb the magnetic field by keeping the steel nails, bolts, nuts and tools away from the spectrometer.

B. Magnet Current Stabilizer

The magnet current stabilizer was originally designed for proton spectrometer for which usually higher current was required than for the beta ray spectrometer. Hence, some parts have been slightly modified to work at the lower currents.

Present section describes our experimental methods applied to check and adjust the stabilizer.

As a start to adjust the stabilizer circuit, the current through a magnet coil is simulated by applying the voltage across 0.5 Ω resistor. A reference voltage is supplied from 6 dry cells (1.5 volts each) through a 50 K Ω helipot. Output pulses of the amplifier circuit at

each stage were observed with oscilloscope to check the amplifier circuit. Fig. 15-19 show the pulse shapes observed after the adjustment. Fig. 15 is the input pulse to the first 5693 tube amplifier with the oscilloscope connected to pin no. 4 of tube 5693 and ground line. Fig. 16 is the pulse shape incoming to the second stage 5693 tube amplifier where the oscilloscope is connected in the same way as in Fig. 15. Input pulse to the third stage 5693 amplifier is shown in Fig. 17. Fig. 18 is the input pulse to the last stage 6V6 tube amplifier circuit where the oscilloscope is connected to pin no. 5 (control grid) of 6V6 tube. The last stage output pulse from 6V6 tube is observed by connecting the scope to pin no. 3 (plate) of 6V6 tube showing the shape something like in Fig. 19. One can see that the pulses are of the regular shape and that the wiggles are smoothened out.

Now, an increase in magnet current should result in decrease in bias on 6AS7 tubes, thus reducing the current through the exciter field. Thus, by measuring the output bias voltage from ½ 6SH7 tube, one can check the amplifier circuit. This is done by varying the voltage on helipot and the voltage across 0.5 Ω resistor with 6SH7 tube in yielding the Table 1.

Unfortunately, the decisive conclusion cannot be extracted out of this table, because of inaccuracy of

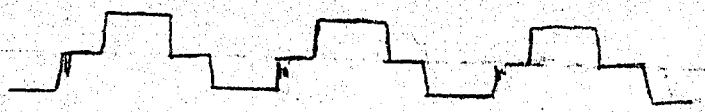

Fig. 15. Input to 1st 5693.

Fig. 16. Input to 2nd 5693.

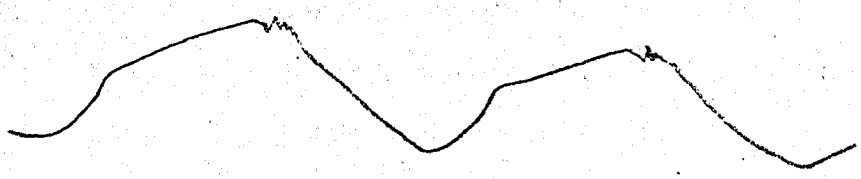

Fig. 17. Input to 3rd 5693.

Fig. 18. Input to 6V6.

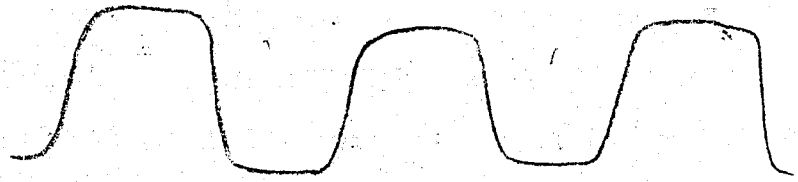

Fig. 19. Output of 6V6.

our experimental set up, but it can be said from the first few columns of this table that the higher the voltage across the 0.5Ω resistor compared to the reference voltage, the lower is the bias voltage of the grids of 6AS7 tubes, which then lowers the current through 6AS7 tubes and adjusts the exciter field.

The stabilizer circuit was then connected to the motor generator and similar readings were taken with the amplifier gain 1 and 8, including the readings of the exciter field current. This is tabulated in Table 2. It is apparent from this table that the stabilizer is working correctly.

Voltage across the 0.5Ω resistor in these experiments is provided by the batteries and the variable resistor connected together, and the Heathkit voltmeter is used to read the voltage drop. Hence the voltage readings are not accurate enough so that it is not possible to reduce the linear relationship between an increase in magnet current and the decrease in the current through the exciter. But still one can see that the increase in voltage across the 0.5Ω resistor compared to the reference voltage results in decrease in exciter field current. Some of the grid bias readings of 6AS7 in Table 2 is inconsistent with the results in Table 1, because of the inaccuracy of the voltmeter readings, etc.

TABLE I

Measurement of grid bias of 6AS7

Voltage across 0.5Ω resistor	Reference voltage	Galvanometer reading	Voltage on pin 1. of 6AL5 with respect to pin 5.	Current through 6SN7 (0-1mA)	Total current (6AL 5 and 6SN7)	Grid bias
1.0	1.00	+4	+1.25	0.08	5.4	-10
1.0	0.95	-2	-1.0	0	5.0	-1.3
1.0	0.90	-10	-3.9	0	4.7	0
1.0	0.85	-18	-5.8	0	4.4	0
1.0	0.80	-18	-6.3	0	4.4	0
1.0	1.05	+10	+4.5	0.2	6.0	-30.5

TABLE 2

Measurement of grid bias and exciter field

gain	reference voltage	0.5Ω volts	grid bias of 6AS7(V)	exciter field current (ampere)
1	1.0	1.00	-34	0.1
1	1.0	0.95	-0.92	3.9
1	1.0	0.90	-0.93	3.8
1	1.0	0.85	-0.93	3.8
1	1.0	1.05	-50	0
1	1.0	1.025	-45	0
1	1.0	~1.000	-23	1.0
1	1.0	~1.000	-11	2.0
1	1.0	~0.975	-4.5	3.0
1	1.0	~1.000	-2.6	3.4
1	1.0	~0.975	-1.3	3.7
8	1.0	~1.000	-2.0	3.6
8	1.0	~1.000	-3.5	3.0
8	1.0	~1.000	-12.0	2.0
8	1.0	~1.000	-22.0	1.0

Two safety devices are provided in order to protect the magnet from any damage. The Weston Sensitrol circuit applies the principle of Wheastone Bridge circuit as shown in Fig. 30. Loeb gives the relation between resistance of pure metals and temperature, to a first approximation

$$R_s = R_o (1 + \alpha t) \qquad (53)$$

where, t is the temperature in Centigrade, and R_o is the resistance of metals at room temperature which, in our case, is 15 Ω when full coil is used. Hence, resistance at $\sim 100^{\circ}C$ is

$$R_s = R_o (1 + \alpha t) = 15 \times (1 + 0.004 \times 85) = 20.1\ \Omega$$

Using the relation for Wheatstone Bridge when galvo. is zero at room temperature,

$$\frac{R_q}{R_p} = \frac{R_x}{R_r} \qquad (54)$$

where, $R_q = 0.5\ \Omega$, $R_p = 20.1\ \Omega$ (at $\sim 100^{\circ}C$),

$$R_r = 167 \times \Omega$$

$$\therefore \quad R_x = \frac{R_q R_r}{R_p} = 5.56 \times \Omega$$

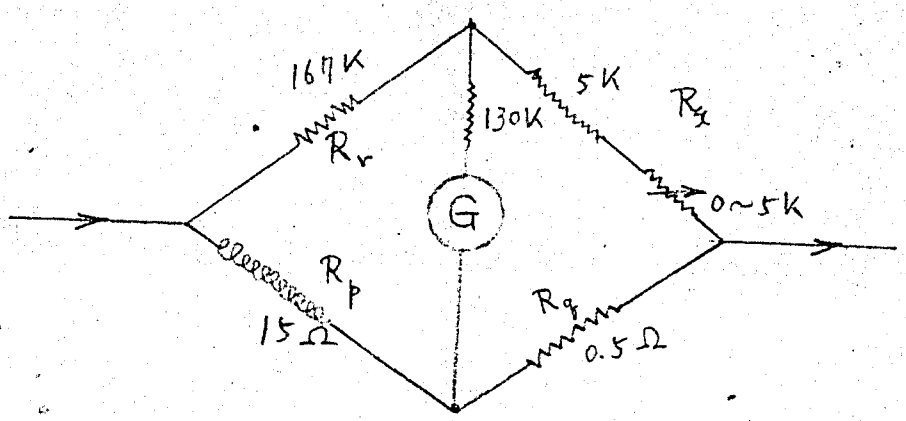

Fig. 20. Wheatstone bridge circuit.

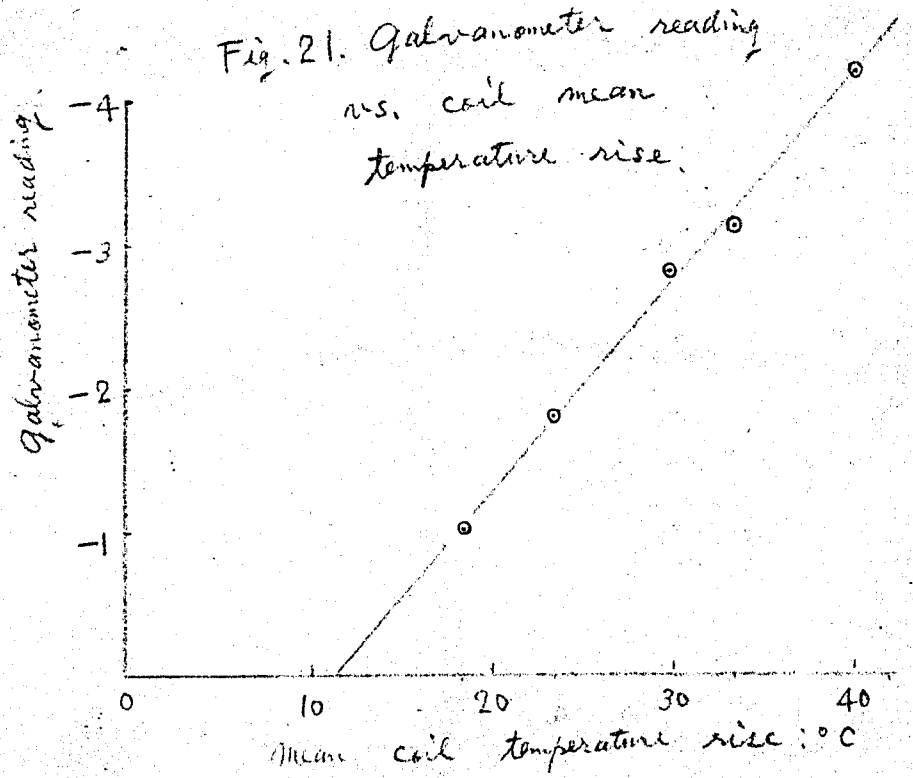

Fig. 21. Galvanometer reading vs. coil mean temperature rise.

Hence, theoretically, the Sensitrol reading should be exactly on zero when the magnet is at room temperature, and when R_x is adjusted to 5.56 K Ω. The experiment is carried out to measure the voltage drop across the magnet, temperature rise of cooling water, and galvanometer readings. Fig. 21, is the relation between galvanometer reading and the mean temperature rise showing that the galvanometer reading varies linearly with mean temperature rise of the magnet. The Tungar cathode is another safety device which provides the short circuit in case of accident in magnet coil circuit. Fig. 22 and Fig. 23, is the general view of our magnet current stabilizer rack and the DC motor generator.

C. Degaussing Coil Systems

Vacuum chamber and magnet coil was fixed to the magnetic N-S direction to minimise the effect of horizontal component of the earth field. Degaussing coils for vertical component of the earth magnetic field was designed and built by myself. Eq. (38) was used to find the number of ampere turns nI, where B should be equal to the vertical component of earth field, i.e., as given on page 16 of the present paper.

$$B = 0.57680 - 0.00020 \times 2.5 = 0.57630 \text{ gauss},$$

and r is the radius of the coil in cm. Since our set up is

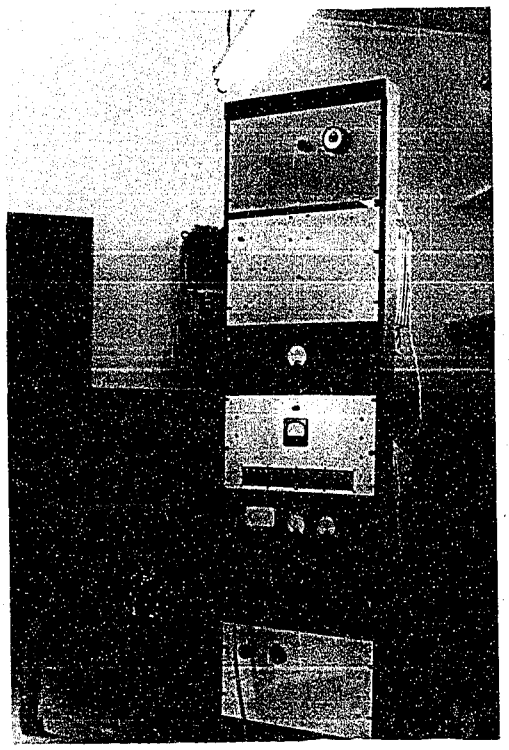

Fig. 22. Stabilizer and Generator

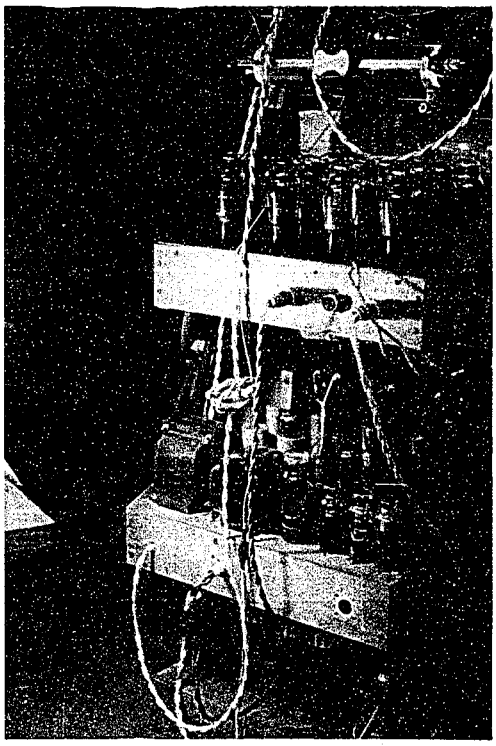

Fig. 23. Current Stabilizer

rectangular frame of 53" x 43", the mean value of r is used, i.e., r = (53" x 43")/2 = 61.8 cm. Hence, nI is found to be

$$nI = \frac{0.5763 \times 61.8}{0.286 \times 3.14} = 39.6$$

assuming I = 1.0 ampere we get

n = 40 turns. Hence 40 turns of gauge 16 copper wire was used in each coil. Total length of wire used is:

(53" + 43") x 2 x 2 x 40 = 1280 feet.

Hence, the resistance of our coil is

4.015 x 1.280 = 5.13 Ω, at 60°F.

This value agreed quite well with the measured value which was 5.1 Ω. Hence voltage drop across the coils must be E = IR = 5.13 volts, when I = 1 amp. Consequently, 4 batteries of 2 volts each were prepared to supply the current. The distance between coils and the axial line of the chamber and the magnt must be equal to r/2 as shown in eq. (36), i.e., r/2 = 30.9 cm. This dimension is applied in our coils. The earth field and effect of the field of

degaussing coils are measured with magnet off, using the 19.8 cm diameter, 608 turns flip coil, and Cambridge fluxmeter. Table 3 shows the fluxmeter reading with the flip-flop coil perpendicular to the vertical line and after quick 180° turn over of the coil. Measurements are repeated at least five times, and average values are tabulated in this table.

It can be seen from Table 3, that the fluxmeter reading -32.8, is equivalent to the vertical component of the earth field, i.e. 0.57630 gauss. Hence, 1 division of fluxmeter reading is equivalent to 0.57630/32.8 = 0.0176 gauss. One can see from Table 3 that 1.12 ampere must be the correct current through the coils, which is consistent with the theoretical prediction. This table also shows that the variation in field by moving the flip-flop coil in the vertical direction is very small agreeing with the theoretical calculation described in Chapter III.

Fluxmeter readings in various conditions

Current through degaussing coils (ampere)	Vertical distance of flip-flop coil from the axial line (cm)	Flip-flop coil reading at the original position	Flip-flop coil reading after 180° turn over	Difference in reading	Field strength (gauss)
0	0	+0.6	-32.2	-32.8	0.57630
1.47	0	+0.8	+5.0	+4.2	0.0740
1.36	0	+0.8	+3.8	+3.0	0.0528
1.18	0	+0.8	+1.3	+0.5	0.0088
1.12	0	+0.9	+1.1	+0.2	0.0035
1.06	0	+0.5	0	-0.5	-0.0088
1.12	2.5	+0.7	+1.2	+0.5	0.0088
1.12	5.0	+0.9	+1.5	+0.6	0.0106
1.12	7.5	+0.9	+1.5	+0.6	0.0106
1.12	10.0	+1.0	+1.9	+0.9	0.0159
1.12	15.0	+0.8	+1.8	+1.0	0.0176
1.12	18.8	+0.8	+1.84	+1.04	0.0183

D. Vacuum Systems

Fig. 24 is the gauge tubes attached to the source end of the vacuum chamber. The left side one is the Pirani gauge which is connected with the chamber, and the center one is the reference gauge. In order to keep these two gauges at the same temperature condition, the two are placed close together. The right side is the ionization gauge which works at the elevated temperature. Hence, in order to avoid the effect of high temperature, the reference gauge of Pirani is placed some distance apart from the ionization gauge. Fig. 25 shows the gauge unit which is attached on the counter rack together with high voltage supply, pulse height analyzer, pulse generator and scaler unit so that one can judge the working conditions easily.

Vacuum is obtained with a "Welch Manufacturing Co." Duo Seal mechanical pump and "Distillation Products, Inc." VMP80 3 stage oil diffusion pump. Before vacuum pumps are switched on, the inside the chamber and fish-eye holder were cleaned up with the volatile chemicals. The mechanical pump is used to pull the system down to a degree of vacuum such that its speed and efficiency decrease rapidly. Between this pump and the chamber is placed an oil diffusion pump which would not function at atmospheric pressure but does begin to work in the pressure region in which the mechanical

Fig. 24. Pirani and ionization gauge tubes.

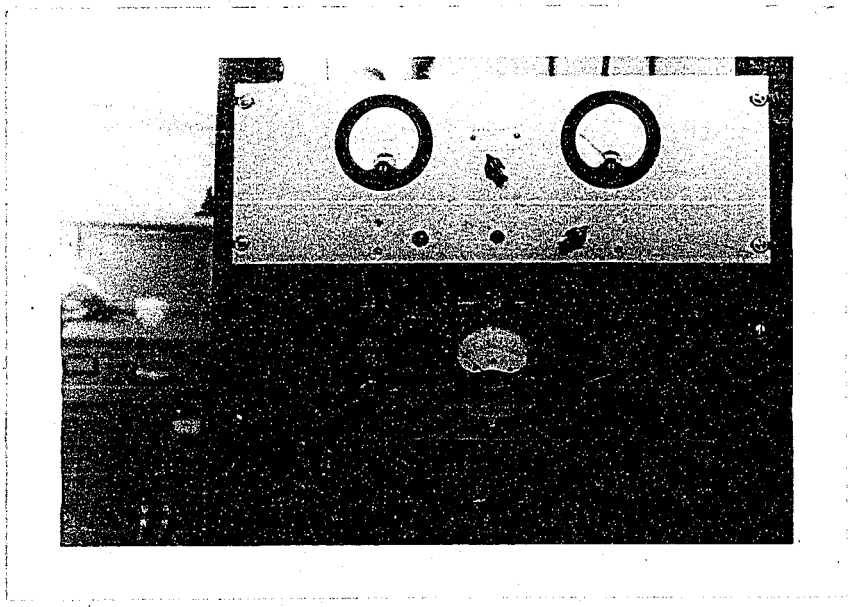

Fig. 25. Pirani gauge and ionization gauge.

pump slows down. Vacuum of 15~10 mmHg is obtained after about 30 minutes run of mechanical pump alone. Fig. 26 shows the function of mechanical pump and diffusion pump on time-ward scale. The best vacuum we attained is 0.022 microns Hg on the ionization gauge reading.

Apieson Q compound is used to seal the flange parts. This compound is found to be quite satisfactory to stop the slight leakage of air.

5. Adjustment of Spectrometer

It is found during the adjustment of the spectrometer that the counting rate is very sensitive to the axial alignment of the vacuum chamber and that of the magnet. Hence, considerably long time is spent to adjust the alignment in order to get the maximum counting rate. A 5 μc Cs^{137} source was used as a calibration source, the diameter of which was 1.2 mm. As a start, the chamber was placed to the magnetic N-S direction as accurate as possible using the stretched string along the axial line. Then, the gap between the surface of the chamber and the magnet was adjusted so that geometrically the chamber and the magnet both lie on about the same axis. The $\frac{1}{2}$ inch baffle opening is provided with 6 inch inner diameter at the center of the chamber. The source distance u and the image distance v are measured giving both 16 5/8" (42.2 cm). Rough dimensions of our spectrometer is given in Fig. 1.

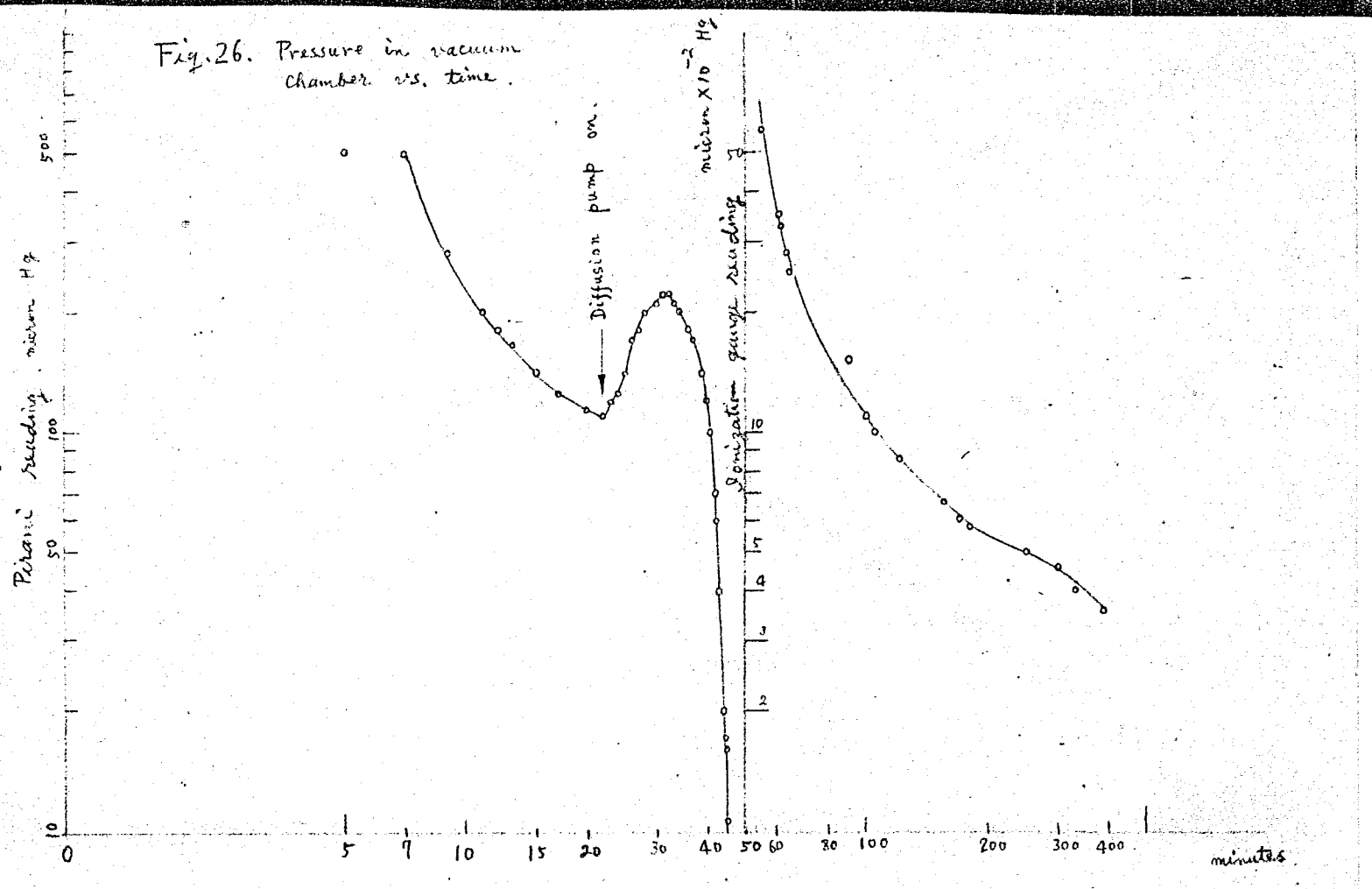
Fig. 26. Pressure in vacuum chamber vs. time.
Pirani reading, micron Hg
500
100
50
10
0
Diffusion pump on.
ionization gauge reading
micron X10 -4 Hg
5
7
10
15
20
30
40
50
60
80
100
200
300
400
minutes

It was found that the counting rate at the magnet current corresponding to L peak of Tm^{170} was much higher when the current through degaussing coils was less than 1.12 ampere, after considerable amount of measurements have been carried out with 2 μc Tm^{170} source in. This did not agree with the theoretical and experimental results on degaussing coils. So, the counting rate is measured by varying the current through degaussing coils with magnet setting at the L peak of Tm^{170} yielding Fig. 27. The curves show that the counting rate reaches to the maximum at 0.6 ~ 0.8 amperes. One can imagine that this might be because of the vertical component of magnet field. This is not impossible because the alignment of chamber and magnet might slightly be off the horizontal plane including the N-S axis, and because the steel diffusion pump might be slightly permanently magnetised from previous use near a spectrometer which was not present during the tests of degaussing coils. Curve 2 on Fig. 27 shows that the curve is shifted after the oscilloscope and chair is moved to the remote place which contained iron.

Hence, another measurement was carried out by setting the degaussing coil at 1.12 amperes, reversing the magnet field and by shifting the magnet to the E-W direction. Curve 1 in Fig. 28 is the one before magnet field is reversed showing continuous decrease in counting rate. By reversing the magnet field, fairly constant and high counting

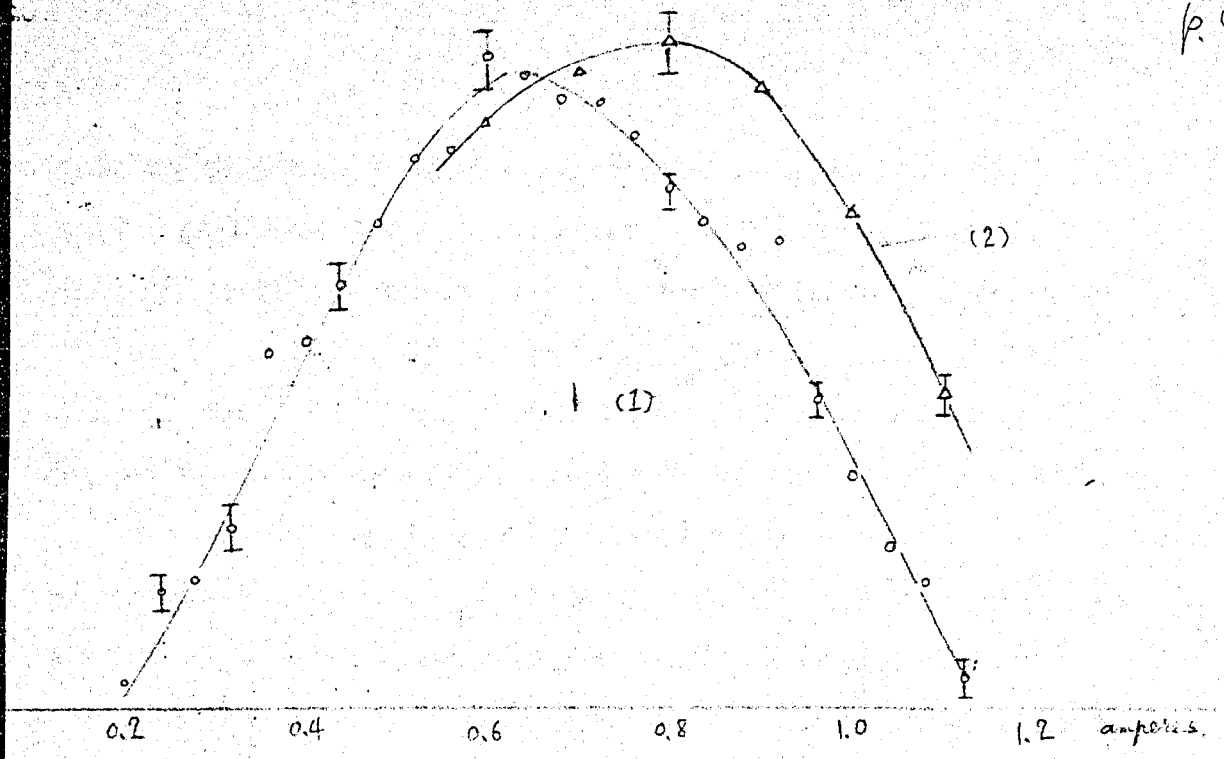

Fig. 27. Count vs. degaussing coil current before the adjustment of spectrometer.

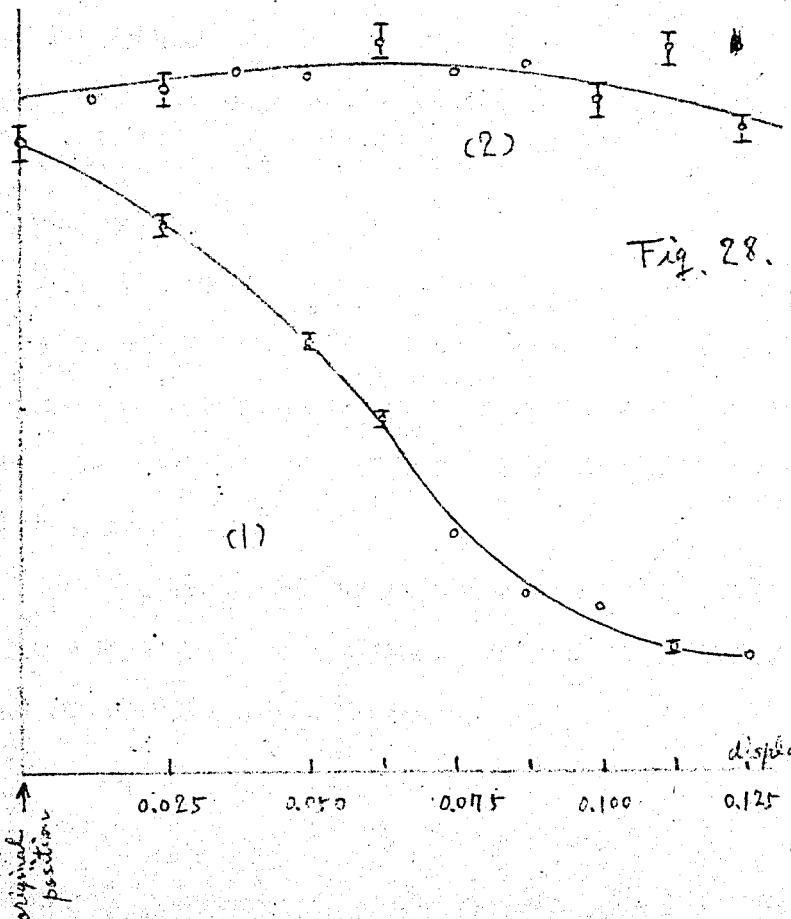

Fig. 28. Counting rate vs. displacement of magnet.

rate is obtained as shown on curve 2 in Fig. 28. The magnet position was fixed at the 0.0625" east from the original position as can be seen from Fig. 28. This is almost the same as the geometrical axis of both chamber and magnet. The final magnet position was found by adjusting the magnet position again in the vertical direction.

According to the data presented by RCA, 1P21 photomultiplier tube can be used with the anode voltage supply up to 1250 volts, but it is found that the tube noise starts at around 700~800 volts. These noise pulses can be discriminated by adjusting the lower bias setting, but unfortunately the pulses from K electron conversion of Yb^{170} are so small that the pulse height from noise and K conversion becomes about the same size. Thus we have to make sure that all the noise pulses are discriminated. This is done by taking the integral bias curve at a few magnet field settings.

Cooling water is supplied to both magnet coil and diffusion pump from the water main line in order to keep the magnet and pump in good working condition. It is observed that coolant temperature difference between inlet and outlet is within 2~3°C.

On the measurement of spectrum, the outer half of the magnet coils only are used in order to minimize the effect of spherical aberration.

F. Calibration of Magnet Current Setting with Cs^{137}

It is found from the measurement of Cs^{137} spectrum that the stabilizer dial setting of 653.3 corresponds to the K line. The K line is 624.2 KeV, and is in momentum, $B\rho$ = 3381 gauss cm.

$$\therefore \quad \frac{3381}{653.3} = 5.19 \text{ gauss cm/division.}$$

Hence, 1 division of stabilizer dial setting is equivalent to 5.19 gauss cm. This is checked with L line where, B = 3500 gauss cm, i.e.,

$$\frac{3500}{676.2} = 5.18.$$

This is in agreement with calibration on the K line.

The excellent agreement of subsequent measurements of the L line of Tm^{170} with the known energy of this line confirmed that the spectrometer was linear and our Cs^{137} K line calibration was reliable.

CHAPTER V

DISCUSSION OF RESULTS

A. Resolution of the Counter

Mainly due to the statistical fluctuations in the number of photons per scintillation incident on the photocathode, and due to the fluctuations in the number of photoelectrons emitted in the photomultiplier, the scintillation counter has finite pulse height resolution. Measurement of the resolution of our scintillation counting instrument is carried out with the aid of the pulse height analyser using a 6% of the peak height. For the K line of Cs^{137} (electron energy = 624.2 KeV) the resolution of the counter at half-width was

$$R_{\frac{1}{2}} = \frac{905 - 660}{783} = 31.3\%$$

Measurement of counter resolution is done simply to check the counting instrument, and the results seem to be satisfactory. In the actual spectrum measurement, the window width is seldom used.

B. Cs^{137}

A) Resolution of Spectrometer.

The resolution of the spectrometer is limited by

slight inaccuracies in alignment, by lens aberrations, by stray magnetic fields, by finite sizes of source and detector, by scattered electrons, and so on. In the energy region with which we are concerned, and in our geometry of source, magnet and detector, the main factors affecting our resolution seem to be (i) slight inaccuracies in alignment and (ii) lens aberrations. Hence, considerable care is taken to get the best chamber, baffle and magnet alignment. Baffle opening was reduced from $\frac{1}{2}$ inch to $\frac{1}{4}$ inch to cut down the effect of lens aberration. Measurement of spectrometer resolution was carried out several times with various set ups. With the best magnet and chamber alignment we could get, a resolution of 3.5% and a transmission of 0.36% (experimental value) were obtained when the baffle gap was set at $\frac{1}{2}$". With 5/16" baffle opening, the resolution and transmission were 3.6% and 0.26% respectively. The best resolution we obtained was with $\frac{1}{4}$" gap and was 2.16%, with an experimental value of transmission of 0.21%. Theoretical prediction of the resolution in this case, is, using eq. (28),

$$R_{\frac{1}{2}} = \frac{S + W}{4R} = \frac{1.2 + 5.5}{4 \times 9 \times 25.4} = 2.20\%$$

This is in agreement with the experimental results.

Approximate transmission calculated from eq. (39) is

$$T = \frac{R\Delta R}{2\mu^2} = \frac{3 \times 2.54 \times 0.25 \times 2.54}{2 \times 41.1^2}$$

$$= 0.15\%$$

This is compared with the experimental results of 0.21% indicating that improved resolution could, if required, have been obtained by a further reduction in the baffle gap ΔR.

B) Spectrum and Resolution Correction.

The spectrum of primary and secondary beta rays from Cs^{137} in the region above 87 KeV examined with the spectrometer resolution of 2.16% in an effort to determine its end point and K, L conversion line. Integral bias curves were taken in both high energy and low energy region to find the correct discrimination level. One minute counts for primary beta ray spectrum, and 2 minutes counts for conversion line were taken. Counting rate at the peak of the spectrum was 613 c/min with standard deviation of ± 25. Background was measured at 2 points i.e., with 3640 gauss cm setting and with magnet current off. Background between these two points are found by extrapolation. Fig. 29 is the observed spectrum of Cs^{137}. The equation

presented by G.E. Owen and H. Primakoff (16) was used to correct the primary beta spectrum close to the end point for resolution,

$$\text{i.e.} \qquad n_c = n_o - \frac{a^2}{4} \frac{d^2 n_o}{dp^2} \qquad (55)$$

where, n_c is the counting rate corrected, n_o is the observed counts and a is the average spread in $B\rho = p$, i.e. half width at half maximum in gauss cm at certain momentum p,

$$\frac{a}{p} = \frac{\Delta p}{2p} = 1.08\%$$

$$\therefore \qquad a = 0.0108 \times p \text{ gauss cm.}$$

Mr. J.M. Robson derived the equation for resolution correction assuming the square resolution curve and gave the same results. $\frac{d^2 n_o}{dp^2}$ is found graphically by taking the tangent line twice.

It is found that the correction is necessary just for a few points close to the end point with the maximum correction of 1 for counting rate of 17 at 498 KeV. End point is estimated roughly from Fig. 29 in enlarged scale for a check, by extrapolation yielding 506.0 KeV. This is compared with the end point obtained from Fermi-Kurie plot.

C) Fermi-Kurie Plot

The forbidden Fermi-Kurie plot of Cs^{137} data, corrected for background and spectrometer resolution is

Fig. 29. Spectrum of Cs^{137}

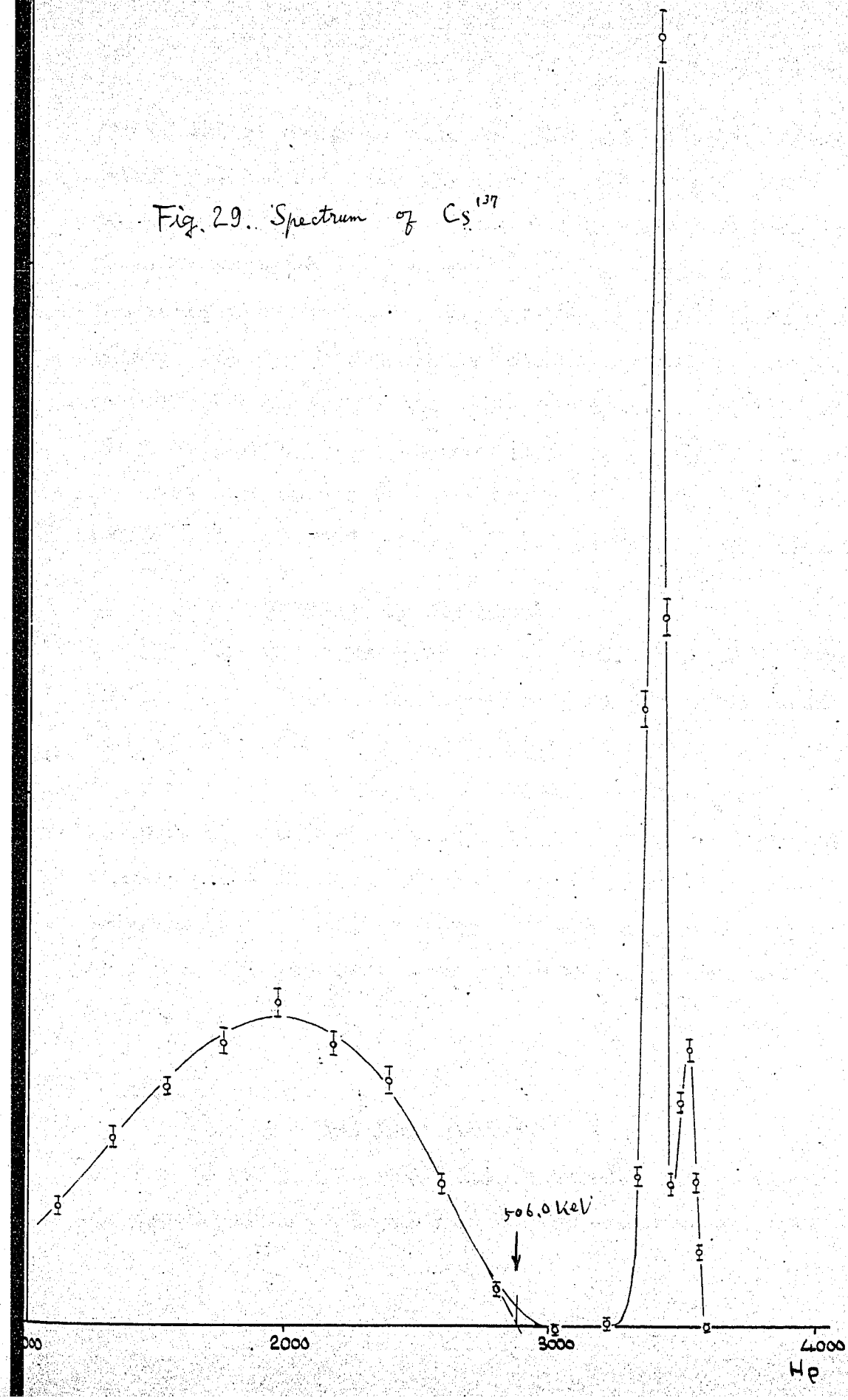

worked out as shown in Fig. 30. The conventional Fermi-Kurie plot did not give the straight line (curve 2a). Correction for forbidden transition is made using eq. (52). Because of the short interval counting, the points are scattered to some extent, and standard deviation, as shown in Fig. 30, for a few points, is quite large. Nevertheless we were able to draw a straight line to find the end point. There are, actually, 2 components of beta spectra, but we were not able to separate the small (8%) high energy component because of poor statistics and high background counting rate.

D) Estimate of End Point.

The end point is found to be 514 ± 5 KeV as shown in F-K plot. This is in agreement with 510 KeV according to R.D. Evans (12). While, L.W. Langer et al. (13) give 510 ± 10 KeV, i.e., our result is within this region. We can say, from this result that the magnetic spectrometer is working correctly, and that our calibration is correct. The drooping in the F-K plot below 150 KeV is to be expected from the foil thickness over the counter and the source thickness.

C. Tm^{170}

A) Spectrum Measurement.

L and M conversion line were measured to check the spectrometer calibration. On the basis of a linear

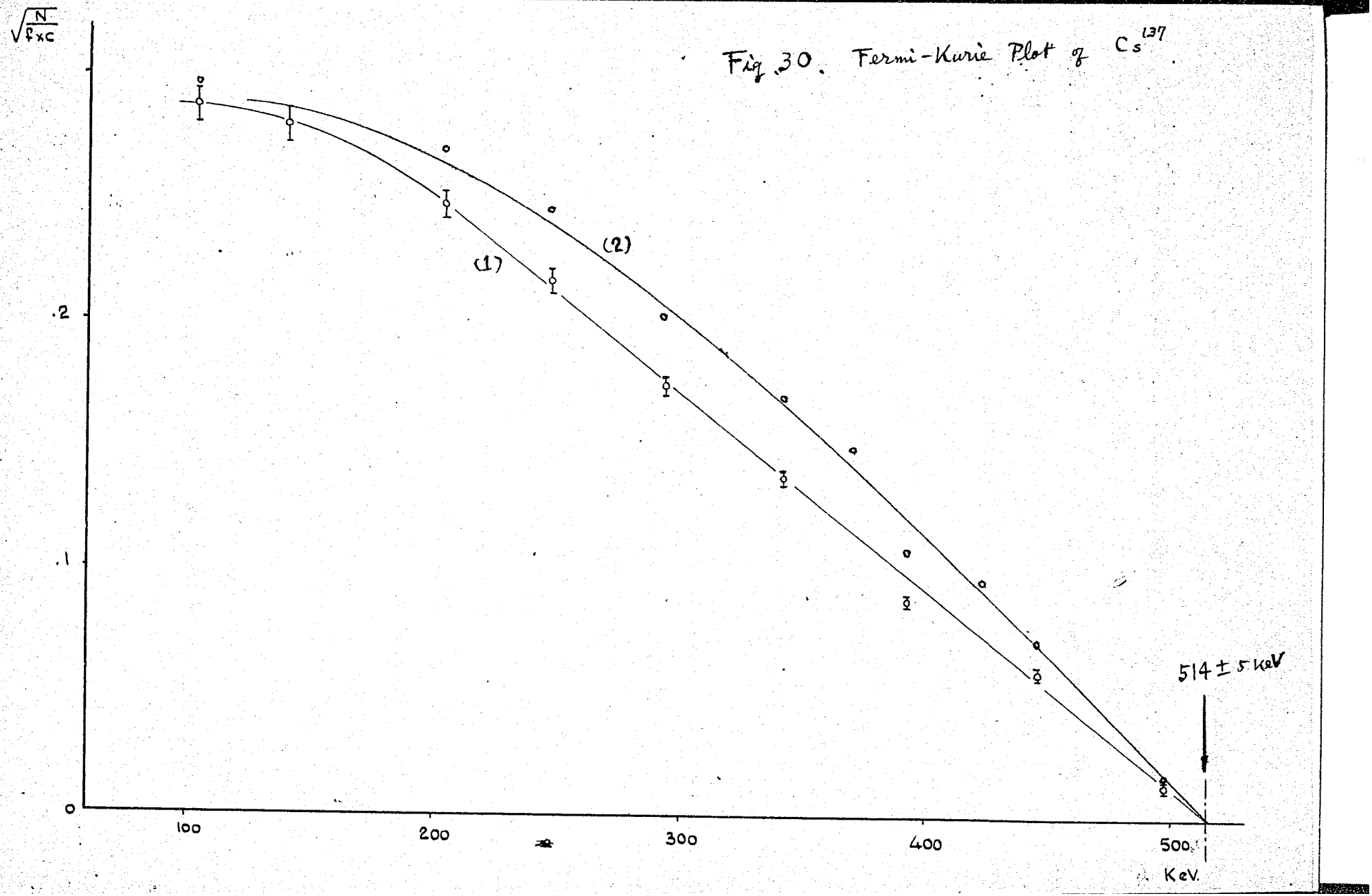

Fig. 30. Fermi-Kurie Plot of Cs^{137}

extrapolation to the Cs^{137} K line calibration, 74.0 KeV (950 gauss cm) for L line and 82.0 KeV (1003 gauss cm) for M line were obtained. J.W. DuMond gives the energy of gamma rays from excited Yb to be 84.26 KeV, and the average binding energies of L and M shell electrons are known to be 9.81 KeV and 1.92 KeV respectively. From these data, we can predict the L and M line to be at 74.45 KeV and 82.34 KeV, respectively. Experimental results agree quite well with these values. The M conversion electrons were not separated from the M line, because of the finite resolution of the instrument.

Integral bias curves were taken with magnet current setting at 950 gauss cm (L line), 1003 gauss cm (M Line) and 3640 gauss cm to find the correct lower bias setting as shown in Fig. 31, and 1.73 V was found to be the correct setting except for the K line. With this bias and with 600 μg/cm^2 aluminum foil over the anthracene crystals, the K conversion line was not detected. The binding energy of K electrons is known to be 61.31 KeV. Hence, 22.95 KeV is the expected K conversion peak. According to the empirical relations worked out by many people, the range of mono-energetic electrons of 22.95 KeV is roughly 900 μg/cm^2 (p. 624, Evans). So, apparently the K electrons are stopped or scattered by the aluminum foil. The K line was measured

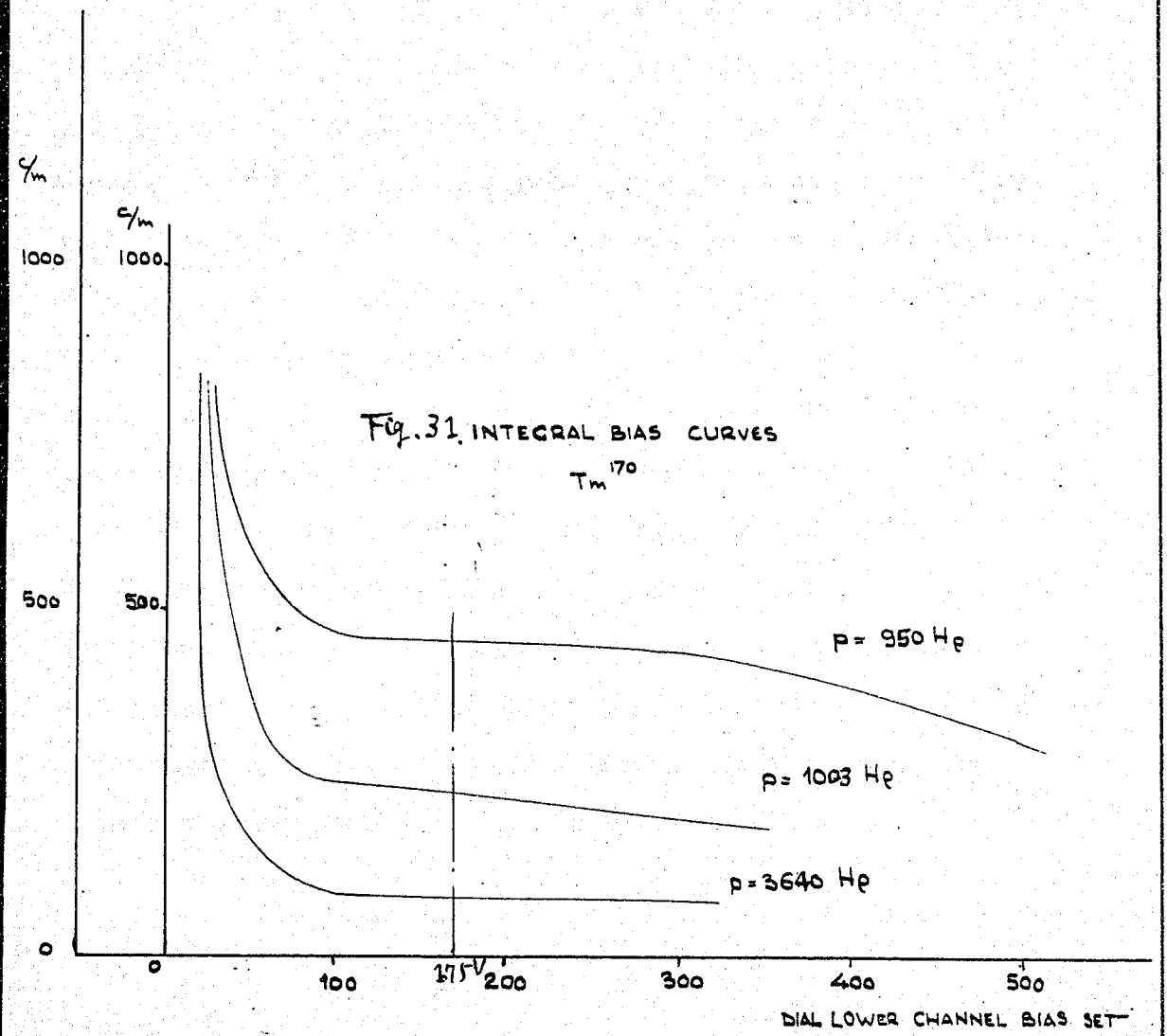

Fig. 31. INTEGRAL BIAS CURVES

Tm^{170}

with aluminum foil of thickness 225 $\mu g/cm^2$, the energy of the monoenergetic electrons corresponding to the range of 225 $\mu g/cm^2$ being approximately 10 KeV, and the K line was then observed at 23.4 KeV (519 gauss cm). This is in reasonable agreement with the predicted energy. The lower bias was set to 1.38V which was found from the integral bias curve as shown in Fig. 32.

The resolution of the spectrometer at the L line is 2.39%. This is higher than the Ca^{137} K peak resolution and would be expected since the electrons from mainly L_{II} and L_{III} shells are combined together with the binding energy of these being slightly different from each other. The resolution at the M line was 2.67%, again expected to be higher due to the presence of the N conversion electrons. Corrections for background and finite resolution of the spectrometer is made in the same way as Cs^{137}. The spectrum is presented in Fig. 33. The measurements are done with 10 minutes count for continuous spectrum except at the peak of the spectrum in an effort to get better statistics. An Auger electron peak is observed between K and L line. Approximate intensity of Auger peak is obtained to be 7% with respect to intensity of L line. This is compared with 2.05% presented by P.R. Gray (19).

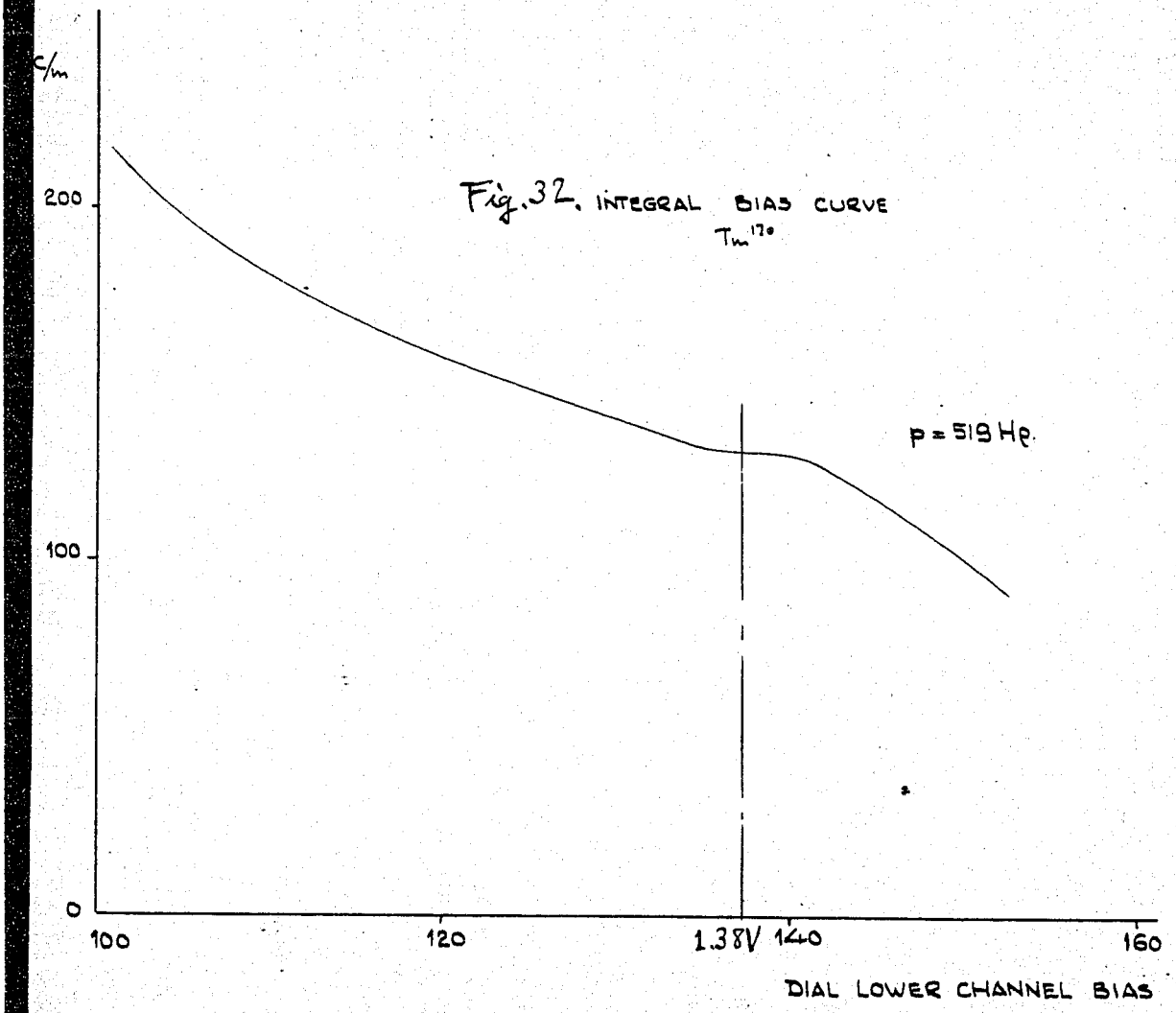

Fig. 32. INTEGRAL BIAS CURVE
T_m 170

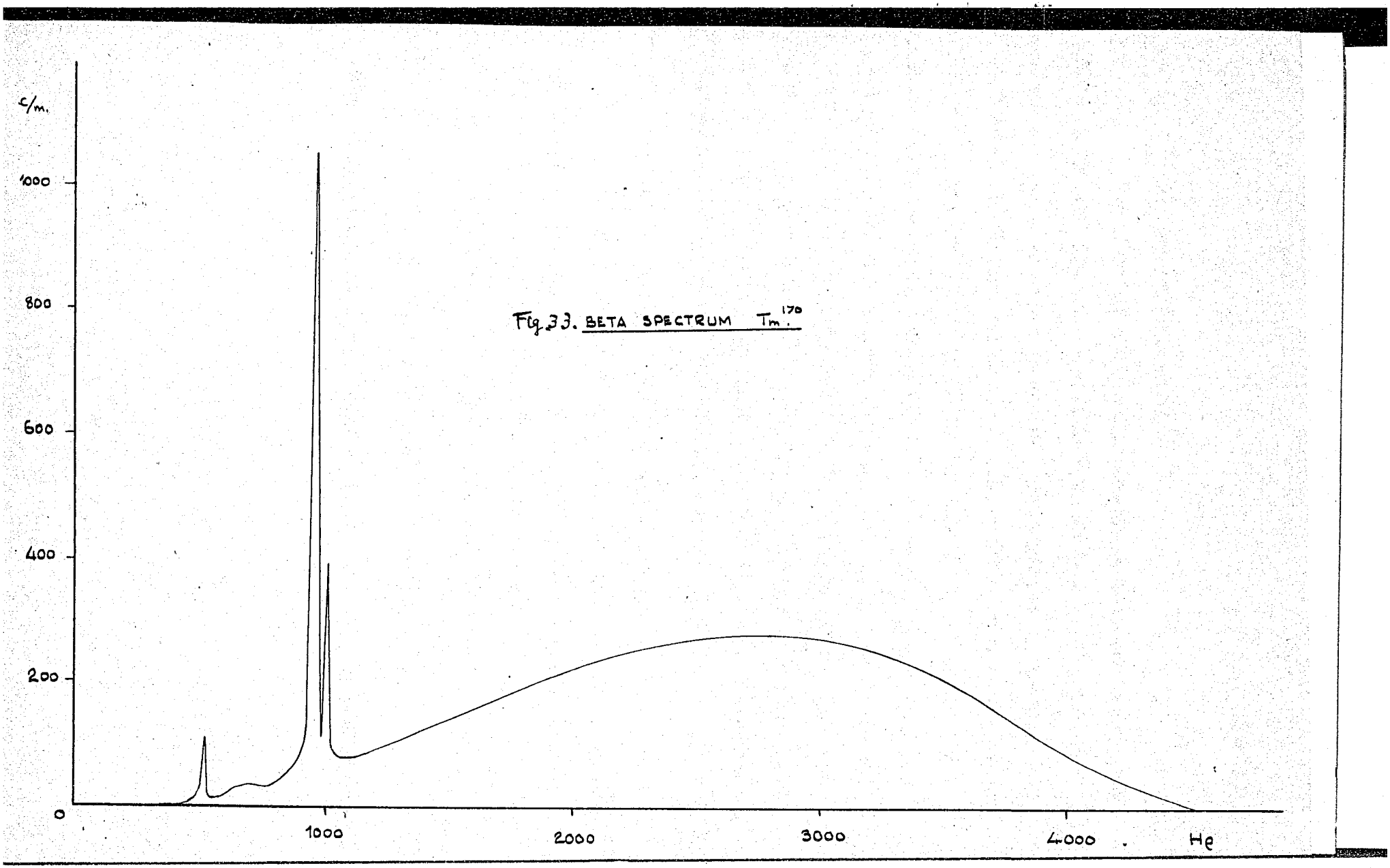

Fig.33. BETA SPECTRUM Tm^{170}.

B) Fermi-Kurie Plot.

F-K plot is worked out assuming allowed transition and given in Fig. 34. According to Graham et al, and A.V. Zohn et al. (18) two components are supposed to be present, but it is found to be difficult to split into two components by extrapolation from our results, since the overall F-K plot turns out to be very nearly a straight line. Much better results would have been obtained if the coincidence techniques were used to split 2 components. Time, however, did not permit this. The end point, from our F-K plot, is 977 ± 9 KeV, which is in agreement with that of the higher energy component given by Graham et al.

C) K:L:M Ratio of Conversion Electrons

The area of the K, L and M peak and of the continuous spectrum were measured from the spectrum in unit momentum interval in the enlarged scale, and the ratio of area of continuous spectrum, K, L, and M peak is obtained to be:

143.2 : 1.65 : 13.05 : 4.07.

This is compared with the Graham et al. and Gray's investigation:

Fig. 7.4. Fermi-Kurie Plot Tm^{170}.

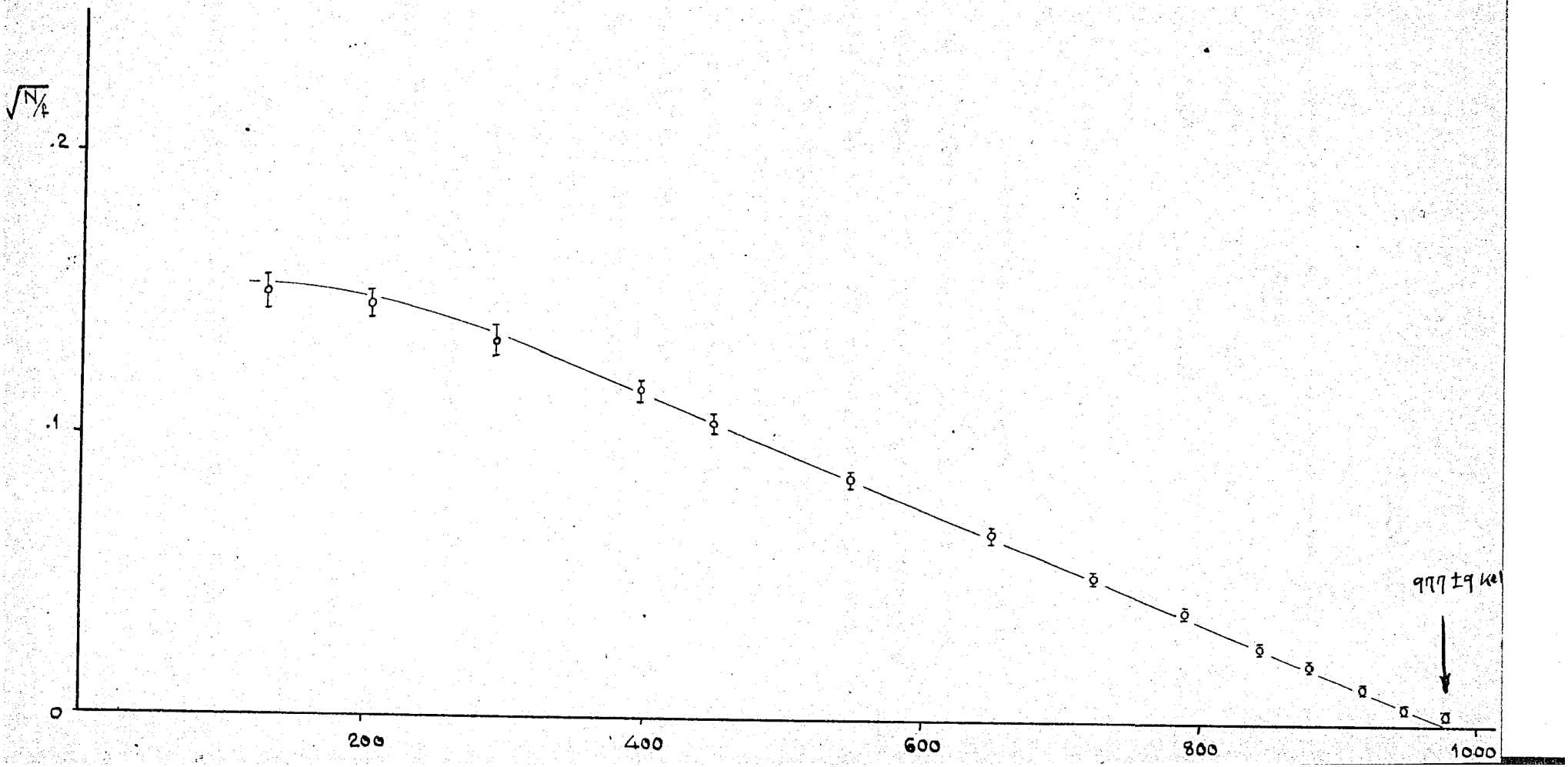

Ratio	Graham et al.	Gray	We
K/L	0.36 ± 0.04	0.32 ± 0.03	0.123
L/M	3.6 ± 0.05	4.3 ± 0.05	3.21
K/L+M	0.28 ± 0.03	0.26 ± 0.03	0.097
K/β	0.045 ± 0.008	-	0.0116
L+M/β	0.16 ± 0.02	-	0.120

Our K/L is considerably lower than the others. This is almost certainly due to absorption in the 225μgm foil over the counter resulting in loss of counts at this low energy by the counter. A higher ratio might have obtained if ~100 $\mu g/cm^2$ aluminum foil was used to cover the scintillator. Besides, this K/L ratio is unreliable because the K conversion electron energy is very close to counter cut off. We will therefore assume our K/L ratio to be in error due to incomplete counting of K electron counts by the counter.

D) Estimate of Conversion Coefficient.

We used the following relation to find the L line conversion coefficient α_L:

$$0.24 \frac{N_B}{N_L} = 1 + \frac{K}{L} + \frac{M}{L} + \frac{1}{\alpha_L} \qquad (56)$$

N_B is the total number of primary electrons, and N_L is number

of electrons corresponding to L line. The ratio $\frac{N_K}{N_L}$, and $\frac{K}{L}$ is obtained from the experimental data. $\frac{K}{L}$ is taken from Graham et al. The factor 0.24 gives the fraction of the decays of Tm^{170} which lead to the excited state of Yb^{170}. We estimate the errors as follows:-

(i) The factor 0.24 is taken from the work of Graham et al, where it was obtained by a coincidence technique. Other workers have obtained 0.23. We therefore take $\pm$ .02 as the error in this quantity.

(ii) The ratio $\frac{N_K}{N_L}$ is obtained by taking a ratio of areas and is subject to uncertainty in estimating the area at the base of the L peak and of the continuum at the low energy end. Estimates from our data on different assumptions indicate an error of $\pm$ 1.9 in this ratio.

(iii) The error in K/L is taken from the work of Graham et al. as $\pm$ .04.

(iv) The error in $\frac{K}{L}$ is estimated as $\pm$ .04.

$$\therefore \quad (.24 \pm .02) \times (10.9 \pm 1.5) = 1 + (0.36 \pm .04) + (0.31 \pm .04) + \frac{1}{\alpha_L}$$

$$\text{giving } \alpha_L = 1.05^{+2.08}_{-0.45}$$

This value is in disagreement with that obtained by Graham et al who used an absolute counting technique. We would expect our value to be low due to

(i) Possible loss of L conversion electrons in the source. There is some evidence for this in the pronounced low energy tail on the L line.

(ii) Non perfect alignment of the spectrometer,

This would be more serious at low energies than at high energies and would tend to make our observed values of L/β low.

(iii) Possible loss of L conversion counts in the counter. This is not expected to be serious as the bias curve appeared to be very flat at this energy.

To resolve this discrepancy further work would be necessary involving a redetermination with a thinner source. The time available for this work (3 months) has not permitted us to investigate this. We conclude that there may be some doubt as to the published values of α_L for Tm^{170} but further work is required to establish this.

CHAPTER VI

CONCLUSIONS

The time available for the experiment was only 3 months, and 2 months were spent to set up and to adjust the spectrometer. Hence, not enough time to investigate the beta decay of Tm^{170} was available.

It was found that the spectrometer was quite linear and our Cs^{137} K line calibration was reliable.

Still better resolution than 2.16% could have been obtained by reducing a baffle aperture by another 1/8"~1/16" without making the transmission too low.

We recommend that the coincidence techniques should be used in order to get the spectrum and the F-K plot of the higher energy component of Tm^{170} beta decay with a high accuracy.

The L line conversion coefficient

$$\alpha_L = 1.05 \begin{matrix} +2.08 \\ -0.45 \end{matrix}$$

is in disagreement with that worked out by Graham et al.

The end point energy of the higher energy component we obtained from the F-K plot (977 ± 9 KeV) is in agreement with the data obtained by Graham et al.

ACKNOWLEDGEMENT

I wish to extend thanks to Dr. P.R. Gendron for the privilege of working in Nuclear Engineering and under his supervision; also for his advice and cooperation throughout our research investigation.

I am especially thankful to Professor J.H. Robson for his extreme patience and guidance which were responsible for my understanding the beta ray spectroscopy.

Finally, I must express thanks and appreciation to AECL and University of Ottawa through whose corporations and facilities were made available to carry out investigation and consequently the writing of this thesis.

BIBLIOGRAPHY

(1) M. Deutsch, L.G. Elliott and R.D. Evans, Rev. Sci. Instr., 15, 178 (1944).

(2) W.B. Fretter, Introd. to Exp. Phys. p. 223 (1954).

(3) G. Fisher, Solid State Phys. Div., N.R.C. Unpublished.

(4) K. Siegbahn, Beta and Gamma Ray Spectroscopy, p. 80, (1955).

(5) L.B. Loeb, Fundamentals of Electricity and Magnetism, p. 59 (1947).

(6) R.D. Evans, The Atomic Nucleus, p. 608 (1955).

(7) R.D. Evans, The Atomic Nucleus, p. 592 (1955).

(8) C.H. Bachman, Techniques in Experimental Electronics, p. 94 (1948).

(9) K. Siegbahn, Beta and Gamma Ray Spec., p. 22 (1955).

(10) J.B. Birks, Scintillation Counters, p. 79, p. 90, (1953).

(11) S.C. Curran, Luminescence and the Scint. Counter, p. 56, (1953).

(12) R.D. Evans, The Atomic Nucleus, p. 232, (1955).

(13) R.L. Graham, I.L. Wolfson and R.E. Bell, Can. J. Phys., Vol. 30, No. 5, p. 459, (Sept. 1952).

(14) "Tables for the Analysis of Beta Spectra", AM13, U.S., N.B.S.

(15) L.M. Langer and H.C. Price, Phys. Rev., Vol. 76, p. 641, (1949).

(16) G.E. Owen and M. Primakoff, Phys. Rev. Vol. 74, p. 1406 (1948).

(17) M.L. De Vries, Thesis, University of Ottawa.

(18) A.V. Pohm, W.E. Lewis, J.H. Talboy and E.N. Jenson, Phys. Rev. vol. 95, p. 1533, (1954).

(19) P.R. Gray, Phys. Rev., Vol. 101, p. 1523 (1954).